



OPEN

Influencing factors and quantitative prediction of gas content of deep marine shale in Luzhou block

Xinyang He^{1,2}, Kun Zhang^{1,2}✉, Shu Jiang³, Zhenxue Jiang^{4,5}, Xueying Wang^{1,2}, Wei Jiang⁶, Jing Li⁷, Yijia Wu⁷, Zhi Gao⁷, Tian Tang⁷, Cheng Yang⁷, Xuejiao Yuan^{1,2}, Fengli Han^{1,2}, Zeyun Wang^{1,2} & Laiting Ye^{1,2}

The exploration and development of deep marine shale gas has made significant breakthroughs, but factors influencing gas contents of deep marine shale are elusive, and quantitative prediction methods of gas content needs to be refined urgently. In this study, the deep marine shale of Longmaxi Formation in Luzhou area was taken as an example, vitrinite reflectance analysis, kerogen microscopy experiment, TOC content analysis, mineral composition analysis, gas content measurement, isothermal adsorption experiment, physical property analysis and argon ion polishing scanning electron microscopy experiment were carried out to find out factors affecting the gas content of deep marine shale, and a gas content prediction model has been worked out. Conclusions below have been reached: the content of adsorbed gas is mainly affected by Ro, TOC content, porosity, water saturation, clay mineral content, formation temperature and pressure; the content of free gas is mainly controlled by porosity, water saturation, formation temperature and pressure; according to the prediction models, the adsorbed gas content, free gas content and total gas content of each well were quantitatively calculated, and the study area was divided into Class I (with a total gas content $\geq 11 \text{ m}^3/\text{t}$), Class II (with a total gas content between $9 \text{ m}^3/\text{t}$ and $11 \text{ m}^3/\text{t}$), and Class III (with a total gas content $< 9 \text{ m}^3/\text{t}$) gas-bearing areas.

Keywords Gas content, Quantitative prediction, Influencing factors, Deep marine shale, Longmaxi formation

Significant progress has been made in the exploration and development of deep marine shale gas ($> 3500 \text{ m}$) in southern Sichuan basin of China in recent years^{1–6}. In Weirong, Dingshan and Luzhou blocks, production capacities on large scale are being constructed. For example, Well Weirong WY23-1, Well Dingye 7HF, Well Lu203, Well Huang202 and Well Zu 202-H1 had gas production rates of 2.601×10^5 , 4.283×10^5 , 1.379×10^6 , 2.237×10^5 and $4.567 \times 10^5 \text{ m}^3/\text{day}$ respectively during formation testing, foretelling deep marine shales have broad prospects of oil and gas exploration and utilization. But Well Yang 101H88-1, Well Yang 101H65-5 and Well Yang 101H56-1 had much lower gas production rates of 7×10^4 , 3.18×10^4 and $10.20 \times 10^4 \text{ m}^3/\text{day}$ respectively in formation testing, namely only 2.31–39.23% (7.42% on average) of that of the high-yield wells mentioned above. Apparently, the deep marine shale strata have wide differences in gas content, adding complication to the development and utilization of shale gas.

Marine shale gas in Southern China mainly occurs in organic-rich shale in two states, adsorbed and free, and changes in occurrence state and gas content with the change of geological environments. The adsorbed gas is adsorbed on the surface of organic matter and clay mineral particles mainly through physical and chemical processes^{7,8}, while the free gas moves freely in pores or fractures formed by tectonism or diagenesis. Shale gas in the study area mainly appears in free state under high temperatures and high pressures of the deep strata^{9,10}.

¹State Key Laboratory of Oil and Gas Reservoir Geology and Exploitation, Southwest Petroleum University, Chengdu 610500, China. ²School of Geoscience and Technology, Southwest Petroleum University, Chengdu 610500, China. ³Key Laboratory of Tectonics and Petroleum Resources (China University of Geosciences), Ministry of Education, Wuhan 430074, China. ⁴State Key Laboratory of Petroleum Resources and Prospecting, China University of Petroleum, Beijing 102249, China. ⁵Unconventional Petroleum Research Institute, China University of Petroleum, Beijing 102249, China. ⁶Shale Gas Exploration and Development Project Department of CNPC Chuanqing Drilling Engineering Company Limited, Chengdu 610051, China. ⁷Institute of Geological Exploration and Development of CNPC Chuanqing Drilling Engineering Company Limited, Chengdu 610051, China. ✉email: shandongzhangkun@126.com

A series of studies on gas contents of shale formations and factors affecting the gas contents have been conducted before^{11–18}. Through isothermal adsorption experiments on low-mature shale samples from Yanchang Formation in Ordos Basin and high-mature shale samples from Longmaxi Formation in Sichuan Basin, Li et al. obtained the contents of shale gas in different occurrence states, and concluded that the continental shales in Yanchang Formation had gas contents between 1.08 m³/t and 2.22 m³/t, low maturity and poor gas-bearing capacity in general; marine shales in Longmaxi Formation had gas contents between 1.23 m³/t to 4.43 m³/t, high maturity and high overall gas-bearing capacity. By analyzing the reservoir characteristics and gas contents of shale samples from Wufeng-Longmaxi Formation of Weirong area in South Sichuan, Xiang et al. suggested that the gas content of shale was jointly controlled by several factors, including TOC content, types and contents of minerals, lithofacies, pore microstructure, fracture and formation pressure. But most of the previous studies were based on isothermal adsorption experiments, in which the maximum adsorbed gas content of shale was calculated by Langmuir isothermal adsorption equation, and the free gas content was calculated by ideal gas equation of state, with only the influences of temperature and pressure on gas content considered. They didn't put forward quantitative prediction models of adsorbed gas content and free gas content by using the main factors affecting the gas content such as organic geochemical properties, mineral content, pore structure, reservoir physical properties, formation temperature and pressure jointly. In some other studies, shale gas contents were measured directly by desorption method on site. But this method requires the experiment to be carried out within 40 min of coring, and the whole experimental process is quite time-consuming and costly, so the gas content can only be evaluated from limited experimental data points.

In this study, the first sub-member of the first member of Longmaxi Formation (the first sub-Mbr in short) in Luzhou block at the southern margin of Sichuan Basin, was taken as the research object. First, the basic characteristics of the target shale layer were identified. Second, the correlations between the adsorbed gas content and free gas content and influencing factors in deep burial conditions were analyzed to screen out main factors affecting them, based on Langmuir equation, multiple linear regression method was used to establish the prediction model of adsorbed gas content under the coupling control of temperature and pressure, and the adsorbed gas contents under different temperature and pressure conditions were calculated by this model. Third, based on the expansion formula of actual gas equation of state, the prediction model of free gas content was established, by which free gas contents under different temperature and pressure conditions were calculated. Finally, the total gas content was worked out, and the favorable areas for exploration were pointed out. The model present in this paper considers the influence of a variety of geological factors on gas content, can continuously calculate gas contents across long shale intervals in wells, overcoming the defect of the original model that can only evaluate from limited experimental data points, and lowering the costs. Moreover, it can improve the evaluation accuracy of gas contents of shale gas reservoirs in the study area and provide a geological basis for evaluation of marine shale gas resources there.

Geological settings

Sedimentary and stratum characteristics

There are two sets of sediments from Wufeng Formation to Longmaxi Formation, i.e., deep-water shelf and shallow-water shelf facies^{19–22}. The Luzhou block was located in the depositional center of deep-water continental shelf during the depositional period of Wufeng Formation-Longmaxi Formation^{23–25}. The Longmaxi Formation here can be divided into three members from bottom to top, namely, the first Mbr, the second Mbr and the third Mbr. And the first Mbr can be subdivided into four sub-Members. The first to third sub-Members are mainly composed of black organic-rich shale with pyrite and calcite bands and are the major production layers rich in shale gas. The fourth Mbr is mainly made up of grayish black shale, with a small number of argillaceous and pyrite nodules^{26–28}.

Tectonic characteristics

The Luzhou Block is located in the low-steep structural zone at the southern margin of the Sichuan Basin. Sandwiched between the Huayingshan fault zone and the Qiyueshan fault zone (Fig. 1), it is jointly controlled by the Huayingshan fault, the Qijiang fault, and the first-order fault of the Qiyueshan fault zone^{29–31}. With strong fold deformations on the whole, it has stronger fold deformation in the northeast, and less stronger fold deformation in the southwest. Specifically, it has narrow and steep anticlines and gentle syncline structures, mainly wide and gentle synclines and low gradient slopes in the southwest, and the synclines and low gradient slopes are over 20 times in area than the anticlines. Transformed by multi-stage tectonic movements, this area has NNE structural belts, SN structural belts and WE structural intersecting with each other, giving rise to multiple thrust faults in NE, near NS and near WE strikes^{32,33}.

Samples, experiments, and data sources

Sample and data sources

A total of 62 samples in this study were taken from the first sub-Mbr of wells Y101H53-3, Y101H4-4, Y101H3-8, Y101H41-2, L203H57-3 and L203H153-8 in Luzhou Block (Table 1). Kerogen type identification, organic matter maturity test, TOC content analysis, mineral composition analysis, porosity test, water saturation test, gas content test, isothermal adsorption experiment and FIB-SEM observation were carried out on these samples. The data of Ro and shale gas contents per unit volume of different members in Sichuan Basin and Xiuwu Basin were also collected from literatures^{34,35}.

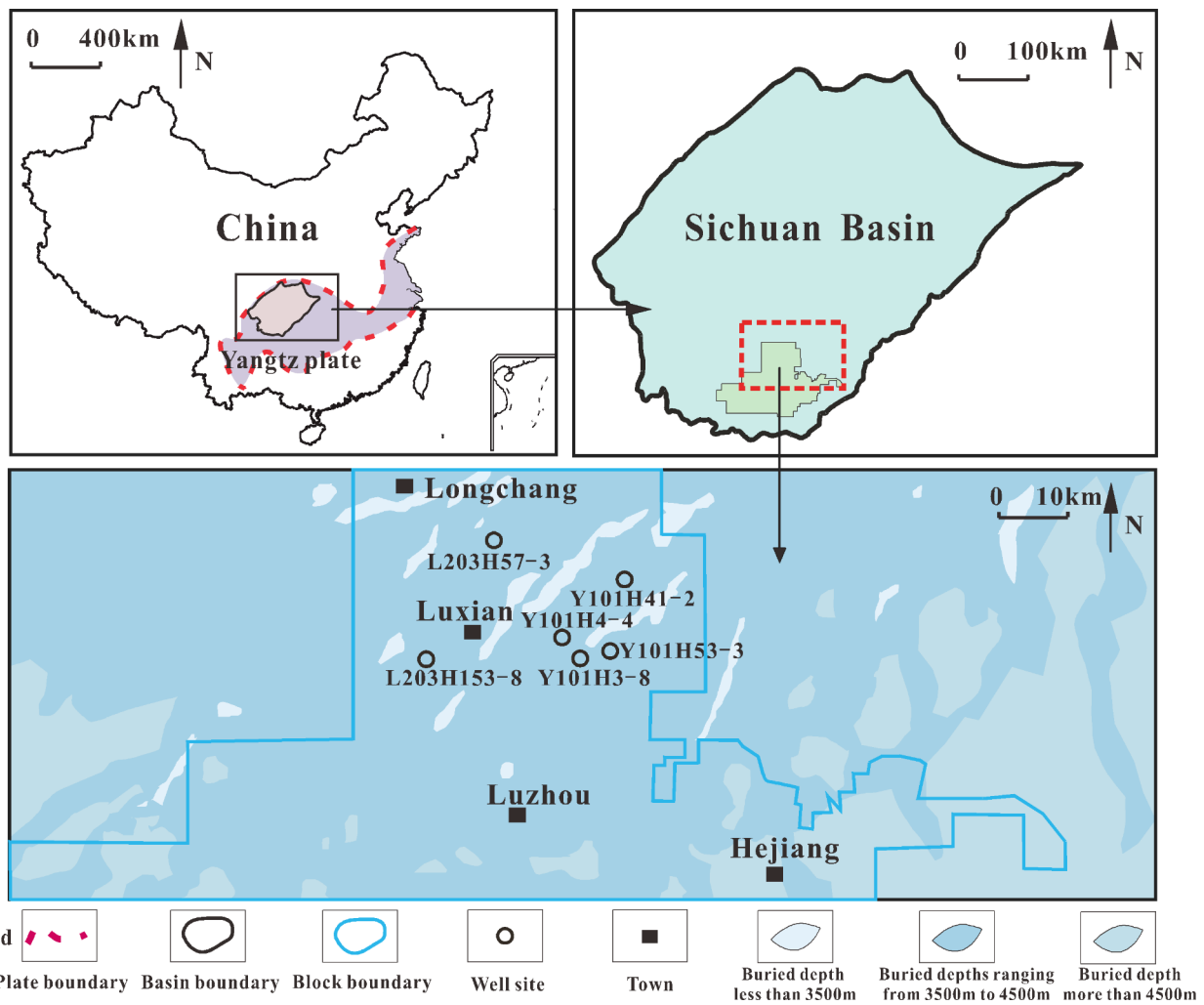


Fig. 1. Location of Luzhou Block in Southern Sichuan Basin, Southern China, and well locations in this block (this figure is generated in CorelDRAW 2020 software, <https://www.coreldrawchina.com/>).

Experimental techniques

TOC content test, kerogen type identification and vitrinite reflectance test

A total of 62 samples were tested for TOC. Each sample was first crushed into powder of 0.2 mm. 0.1 g of the powder was treated with sufficiently diluted hydrochloric acid to remove carbonates, then what was left was washed and dried, and finally the total organic carbon (TOC) content was measured with an OG-2000 V carbon and sulfur analyzer.

Kerogen types of the 62 samples were identified. The method was as follow: firstly, the slice of a wet kerogen sample of each sample was prepared; secondly, microscopic components of the slice were identified by using transmitted light and reflected fluorescence of a ZEISS fluorescence microscope Axio Scope with total magnifications set at 400 times to 600 times; and finally, the microscopic components were identified according to their optical characteristics, each sample was scanned and observed under a certain magnification to count the sample particles entering a fixed coordinate.

The vitrinite reflectances of 10 samples were measured. Each sample was crushed into particles of 20–40 meshes, the particles were with epoxy resin, after solidification, the mixture was pressed into a slice and polished, and then the marine vitrinite in the shale sample was observed by using an oil immersion objective lens with a magnification of 50.

Analysis of mineral composition

All the 62 samples were analyzed by XRD. Each sample was crushed into powder of 40 μm grain size, and then analyzed by CoK α radiation with an Ultima IV X-ray diffractometer. The diffracted beam scanned in the sample powder at a rate of 2° (2θ)/min over a range of 3° to 85° (2θ), and the percentages of minerals were then determined by estimating the areas of their corresponding peaks in the spectrogram.

Number	Well	Formation	Depth (m)	Number	Well	Formation	Depth (m)	Number	Well	Formation	Depth (m)
1	L203H57-3	Longmaxi	3717.36	12	Y101H41-2	Longmaxi	4065.40	23	Y101H4-4	Longmaxi	4097.87
2	L203H57-3	Longmaxi	3718.34	13	Y101H41-2	Longmaxi	4066.77	24	Y101H4-4	Longmaxi	4098.92
3	L203H57-3	Longmaxi	3719.42	14	Y101H41-2	Longmaxi	4067.41	25	Y101H4-4	Longmaxi	4099.85
4	L203H57-3	Longmaxi	3720.40	15	Y101H41-2	Longmaxi	4068.80	26	Y101H4-4	Longmaxi	4101.04
5	L203H57-3	Longmaxi	3721.32	16	Y101H41-2	Longmaxi	4069.62	27	Y101H4-4	Longmaxi	4102.00
6	L203H57-3	Longmaxi	3722.23	17	Y101H41-2	Longmaxi	4070.69	28	Y101H4-4	Longmaxi	4103.08
7	L203H57-3	Longmaxi	3723.03	18	Y101H41-2	Longmaxi	4071.61	29	Y101H4-4	Longmaxi	4104.06
8	L203H57-3	Longmaxi	3724.29	19	Y101H41-2	Longmaxi	4072.78	30	Y101H4-4	Longmaxi	4105.10
9	L203H57-3	Longmaxi	3725.46	20	Y101H41-2	Longmaxi	4073.55	31	Y101H53-3	Longmaxi	4021.84
10	L203H57-3	Longmaxi	3726.43	21	Y101H4-4	Longmaxi	4095.68	32	Y101H53-3	Longmaxi	4022.66
11	Y101H41-2	Longmaxi	4064.54	22	Y101H4-4	Longmaxi	4096.84	33	Y101H53-3	Longmaxi	4023.68
34	Y101H53-3	Longmaxi	4024.62	45	L203H153-8	Longmaxi	4058.36	56	Y101H3-8	Longmaxi	3709.70
35	Y101H53-3	Longmaxi	4025.57	46	L203H153-8	Longmaxi	4059.37	57	Y101H3-8	Longmaxi	3711.64
36	Y101H53-3	Longmaxi	4026.86	47	L203H153-8	Longmaxi	4060.35	58	Y101H3-8	Longmaxi	3713.59
37	Y101H53-3	Longmaxi	4027.60	48	L203H153-8	Longmaxi	4061.31	59	Y101H3-8	Longmaxi	3715.28
38	Y101H53-3	Longmaxi	4028.45	49	L203H153-8	Longmaxi	4062.32	60	Y101H3-8	Longmaxi	3717.74
39	Y101H53-3	Longmaxi	4029.64	50	L203H153-8	Longmaxi	4063.31	61	Y101H3-8	Longmaxi	3719.96
40	Y101H53-3	Longmaxi	4030.70	51	Y101H3-8	Longmaxi	3699.50	62	Y101H3-8	Longmaxi	3722.30
41	L203H153-8	Longmaxi	4054.35	52	Y101H3-8	Longmaxi	3701.57				
42	L203H153-8	Longmaxi	4055.38	53	Y101H3-8	Longmaxi	3703.57				
43	L203H153-8	Longmaxi	4056.37	54	Y101H3-8	Longmaxi	3705.53				
44	L203H153-8	Longmaxi	4057.39	55	Y101H3-8	Longmaxi	3707.45				

Table 1. No., well names and horizons of the tested samples, see Fig. 1 for the well locations.

FIB-SEM observation

Six samples were observed by FIB-SEM. Before the scanning electron microscopy (SEM) observation, each sample was prepared into a regular cube of 1 cm × 1 cm × 1 cm, and the surface to be observed was polished by argon ion. The FEI HELIOS NANOLAB 650 SEM, with a minimum resolution of about 1 nm, was used to observe the samples, to get the two-dimensional structure characteristics of shale micro-nano-scale pores, and the mineral types were identified by EDAX energy spectrometer.

Isothermal adsorption experiment

Isothermal adsorption experiments were carried out on 42 samples with a FY-KT 1000 isothermal adsorption apparatus. Firstly, each sample was ground into powder with a diameter of 0.25 mm, and the mass and volume of the adsorption tank were measured by Archimedes method with nitrogen as the fluid. The sample was then crushed into 60–80 mesh powder, and the powder sample was dried and degassed at 110 °C for 8 h to remove water and impurity gases. Then the powder sample was put into the adsorption tank, and its mass and particle volume were measured with helium as the fluid. Finally, methane with the purity of 99.99% was used as adsorbent, and methane excess adsorption isotherms at 16 pressure points ranging from 0.5 to 30 MPa at 125 °C were measured.

Tests of porosity and water saturation

All the 62 samples were tested for porosity and water saturation. A DQKY-I Full diameter plunger core porosity tester was used to measure the porosity. The measurement process was as follows: a core plug was put into the sample chamber for vacuumizing, and the pressure (P1) of the sample chamber was recorded; helium was injected into the reference chamber, and after the pressure balanced, the gas pressure (P2) in the reference chamber was recorded; the reference chamber was connected with the sample chamber to fully saturate the sample pores with helium gas; after the pressure balanced, the gas pressure (P3) in the sample chamber was recorded, the shale sample skeleton volume was obtained by conversion of Boyle's law, and then in combination with the total volume of the sample, the shale porosity was calculated. During the experiments, the accuracy of the pressure sensor was no less than 0.1 FS, and the purity of helium was more than 99.9%.

The liquid saturation method was adopted to measure the water saturation. The steps were as follows: a shale sample was weighed and then dried in an oven, then weighed in the air, and the mass difference of the shale rock sample before and after drying was divided by the density of water to obtain the volume of water containing in the shale sample. Then the dried shale rock sample was put into a vacuum pressure tank and vacuumized to 6×10^{-2} Pa. The vacuum pressurization tank was filled with liquid to saturate the sample at the pressure of 20 MPa for more than 24 h. Finally, with the liquid on the surfaces wiped off, the saturated shale sample was weighed in the air. The difference between the mass weighed in the air and the mass of the dried shale sample was divided by the density of the saturating liquid to obtain the pore volume of the shale sample, and the percentage of water volume in the pore volume was taken as the water saturation of the shale sample.

Results and models validation

Basic characteristics of the shale samples

Maturities and types of organic matter

Results of vitrinite reflectance experiments on the shale samples show that their organic matter Ro values range from 3.03 to 3.37%, with an average of 3.20%, and mostly fall in between 3.20% and 3.30%, showing the shale samples are of high thermal evolution degree, and in over-mature stage with abundant organic matter pores, mainly generating dry gas. The results of composition identification of the shale samples show they have type indexes of kerogen from 93.0 to 98.3, with an average of 96.8, suggesting they contain largely type I organic matter (Table 2).

Mineral composition and physical property characteristics

With the increase of burial depth, the content of siliceous minerals increases, while the contents of clay minerals and carbonate minerals decrease. Siliceous minerals accounts for 44.98% on average, of which quartz and plagioclase take up 38.60% and 6.38% respectively. Clay minerals make up 32.51% on average, of which, illite, chlorite, kaolinite and montmorillonite account for 22.49%, 5.06%, 3.39% and 1.57% respectively. Carbonate minerals account for 18.49% on average, of which dolomite and calcite are 10.84% and 7.65% respectively. And pyrite only takes up 4.02%. The shale samples have TOCs of 1.47–5.35%, on average 2.89%, and TOCs increasing with the burial depth, indicating they have high organic carbon contents and high hydrocarbon generation potential^{36,37}. The samples have porosities and water saturations increasing with the increase of buried depth. They have a porosity range from 1.80 to 6.17%, and an average porosity of 4.58%; a water saturation range from 4.16 to 52.63%, and an average water saturation of 24.77% (Fig. 2).

Pore types

According to the composition of shale matrix, the pores in the study area were divided into organic pores and inorganic pores. The organic pores are mainly pyrobitumen pores (Fig. 3a, e), and occasionally solid kerogen pores (Fig. 3b)^{38–41}. The inorganic pores can be divided into intergranular pores and intragranular pores, both of which appear in siliceous, carbonate and clay minerals (Fig. 3a–f). On the whole, organic pore is the main type in the study area, and inorganic pores are underdeveloped.

Analysis on factors influencing gas content of the shale

Microscopic occurrence mechanisms of shale gas

Adsorption is the molecular aggregation process of gas molecules on solid surfaces caused by surface energy minimization^{9,10,42}, and methane adsorption by coal seams of high temperatures and high pressures belongs to physical adsorption⁴². Under the experimental conditions, the adsorption process of methane by organic-rich shale is a reversible reaction, and methane can completely desorb through depressurization process, and the adsorption and desorption are fast. Previous calculations show that the mud shale, kerogen and clay minerals have low equivalent adsorption heat to methane between 7.3 and 28 kJ/mol; and in the range of several times of coagulation heat (9.01 kJ/mol), different types of shale, different types of kerogens at different maturities, and different types of clay minerals all show good linear relationships between standard adsorption entropy and equivalent adsorption heat^{9,43–45}. Therefore, the adsorption of methane by high-temperature and high-pressure shale also belongs to physical adsorption caused by van der Waals force, and its essence is the mutual attraction between surface molecules of organic matter and inorganic mineral particles, and methane molecules through van der Waals force.

In molecular dynamics, the interaction energy between molecules can be simulated by the Lennard–Jones potential energy function. The Lennard–Jones potential energy function, with the distance between molecules as the only variable and two parameters, is expressed as^{46,47}:

$$V(r) = 4\epsilon \left[\left(\frac{\sigma}{r} \right)^{12} - \left(\frac{\sigma}{r} \right)^6 \right] \quad (1)$$

The intermolecular force counter to the Lennard–Jones potential is:

Formation	Depth (m)	Ro (%)	Kerogen type index
Longmaxi	4095.68	3.10	96.4
Longmaxi	4096.84	3.15	95.7
Longmaxi	4097.87	3.11	96.0
Longmaxi	4098.92	3.03	97.7
Longmaxi	4099.85	3.20	93.0
Longmaxi	4101.04	3.24	96.8
Longmaxi	4102.00	3.30	98.2
Longmaxi	4103.08	3.37	97.5
Longmaxi	4104.06	3.27	98.3
Longmaxi	4105.10	3.23	98.4

Table 2. Analysis results of vitrinite reflectance and kerogen type of well Y101H4-4.

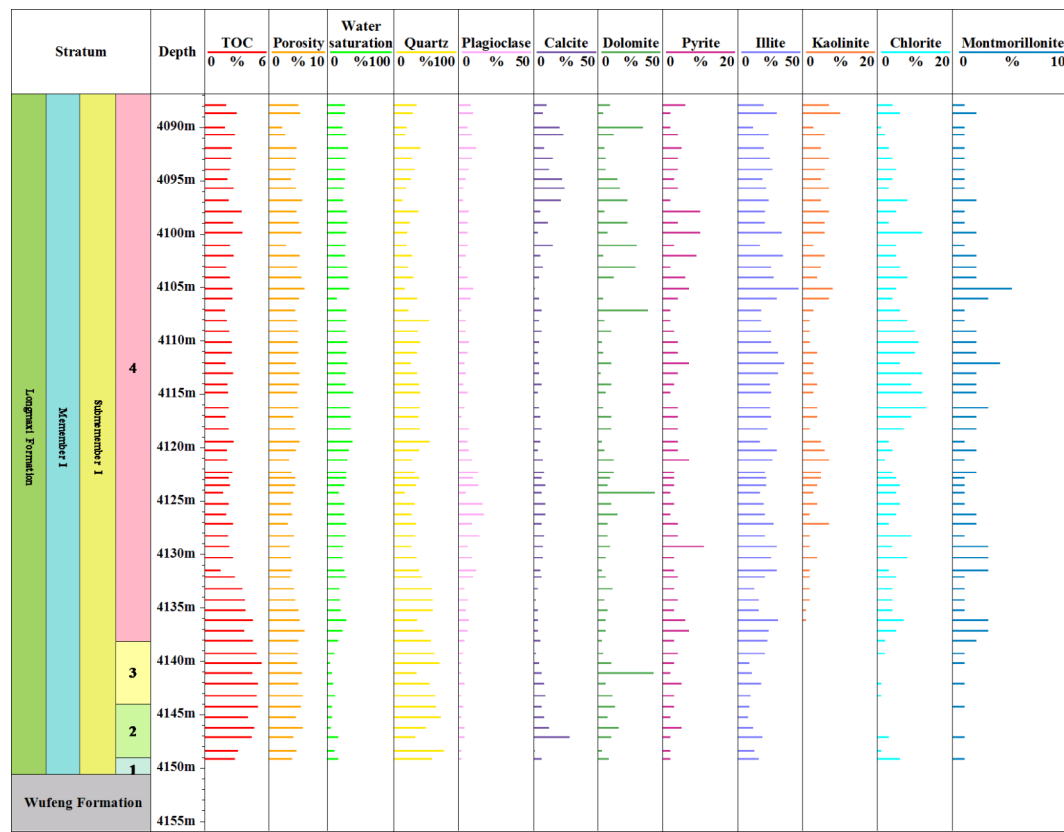


Fig. 2. Assay and test results of shale samples from Well Y101H4-4.

$$F(r) = -\nabla V(r) = -\frac{d}{dr}V(r)\hat{r} = 4\epsilon \left[\frac{\sigma^{12}}{r^{13}} - 6 \left(\frac{\sigma^6}{r^7} \right) \right] \hat{r} \quad (2)$$

where V is the intermolecular potential energy; F is the intermolecular force; r is the distance between molecules; ϵ is the energy scale (potential well depth); σ is the distance scale (Fig. 4).

Based on the van der Waals force, the microscopic occurrence state of shale gas can be found out by calculating the potential well distance with Lennard-Jones potential energy function (Fig. 5). There are attractive and repulsive forces between molecules, and the resultant force of the two is the van der Waals force. Both the attractive force and repulsive force decrease with the increase of distance between molecules, and increase with the decrease of distance between molecules, moreover, the repulsive force varies faster than the attractive force. When the pore diameter (d) is less than $20r_0$ (van der Waals radius) and the distance between the methane molecule and the pore wall molecule is less than $10r_0$, there exists van der Waals force, and the methane molecule is attracted to the equilibrium position by the pore wall molecule and is thus in adsorption state. When the pore diameter (d) is greater than $20r_0$ and the distance between the methane molecule and the pore wall is greater than $10r_0$, there is no Van der Waals force between the molecule of the pore wall and the methane molecule, and the methane molecule can diffuse freely and is in free state. Therefore, only adsorbed methane molecules exist in tiny nanopores (with pore diameters d of less than $20r_0$), and $20r_0$ is the critical pore diameter for the occurrence of free methane^{48,49}.

Free shale gas exists in the pores or fractures of shale and can flow freely. The amount of free shale gas depends on the free space inside the shale. When enough gas molecules are adsorbed on the mineral surface, the excess gas molecules exist in the pores and fractures of the rock in free state. The gas in free state can be described by the gas equation of state, for the ideal gas, the state equation is:

$$PV = nRT \quad (3)$$

In practical applications, the ideal gas equation of state can be corrected by the compressibility coefficient:

$$PV = znRT \quad (4)$$

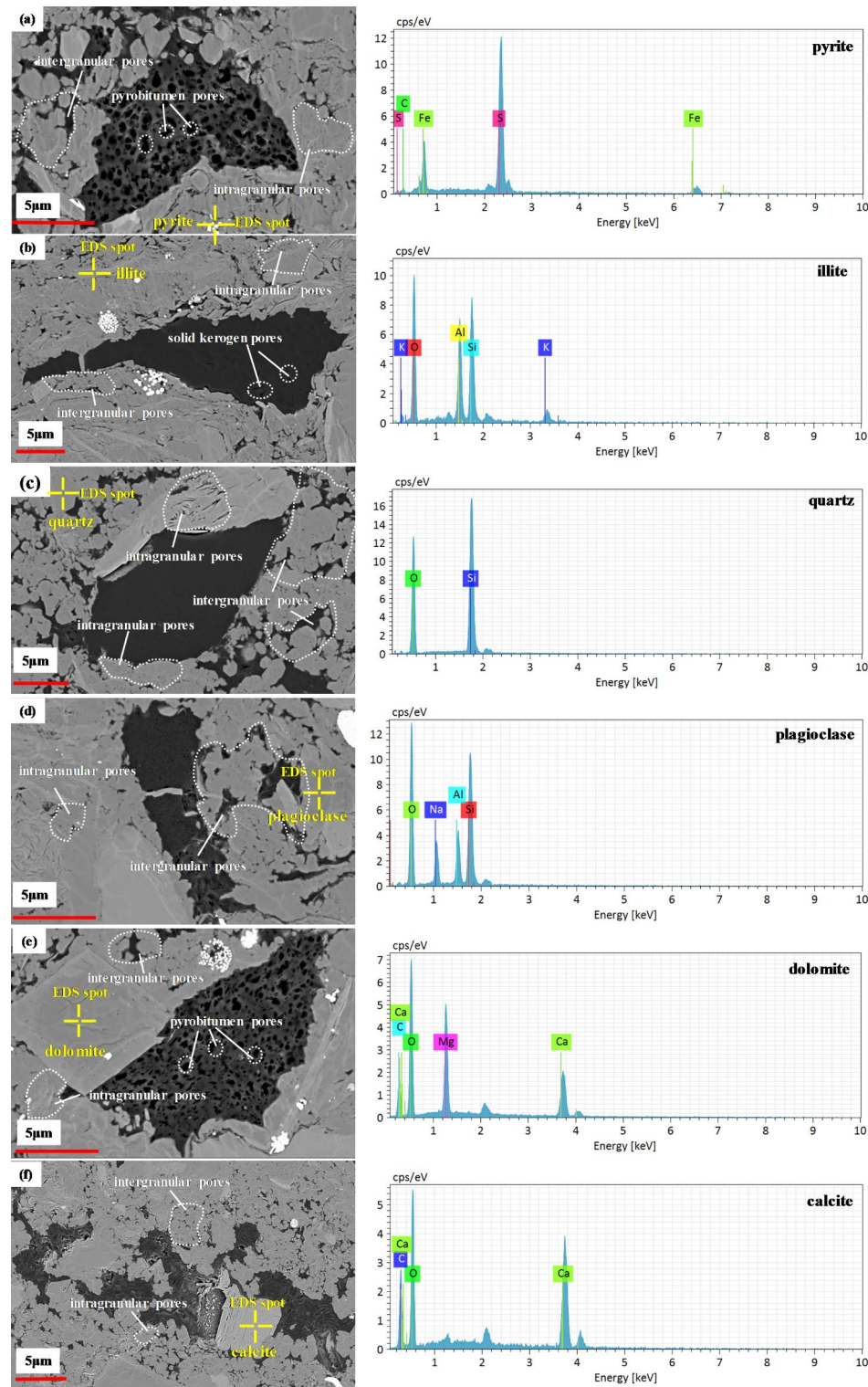


Fig. 3. Pore types and mineral types.

where P is pressure of the gas, MPa; V is volume of the gas, cm^3 ; n is the amount of the gas, mol; T is the thermodynamic temperature of the gas, K; R is the ideal gas constant, 8.314; Z is the gas compressibility coefficient.

The amount of free gas depends on the pore volume, temperature, gas pressure, and gas compressibility. With the rise of pressure, the volume of gas will become smaller, so the free gas contained in a certain pore space

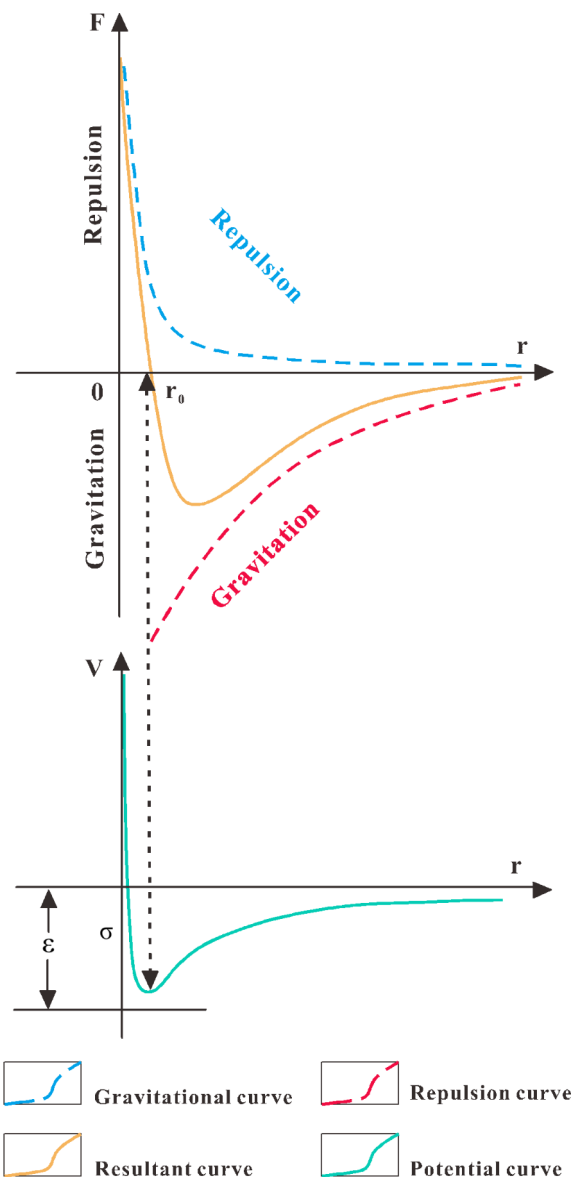


Fig. 4. Schematic diagram of intermolecular forces^{46,47}.

will increase. After enough methane molecules are adsorbed, part of the shale gas occurs in dissolved state in kerogen, asphalt and water. The dissolution mainly appears in the form of gap filling and hydration⁵⁰. When coming into contact with liquid hydrocarbons, shale gas molecules enter the interstices between hydrocarbon molecules such as kerogen and bitumen due to molecular diffusion. The amount of dissolved gas in shale is small and usually negligible.

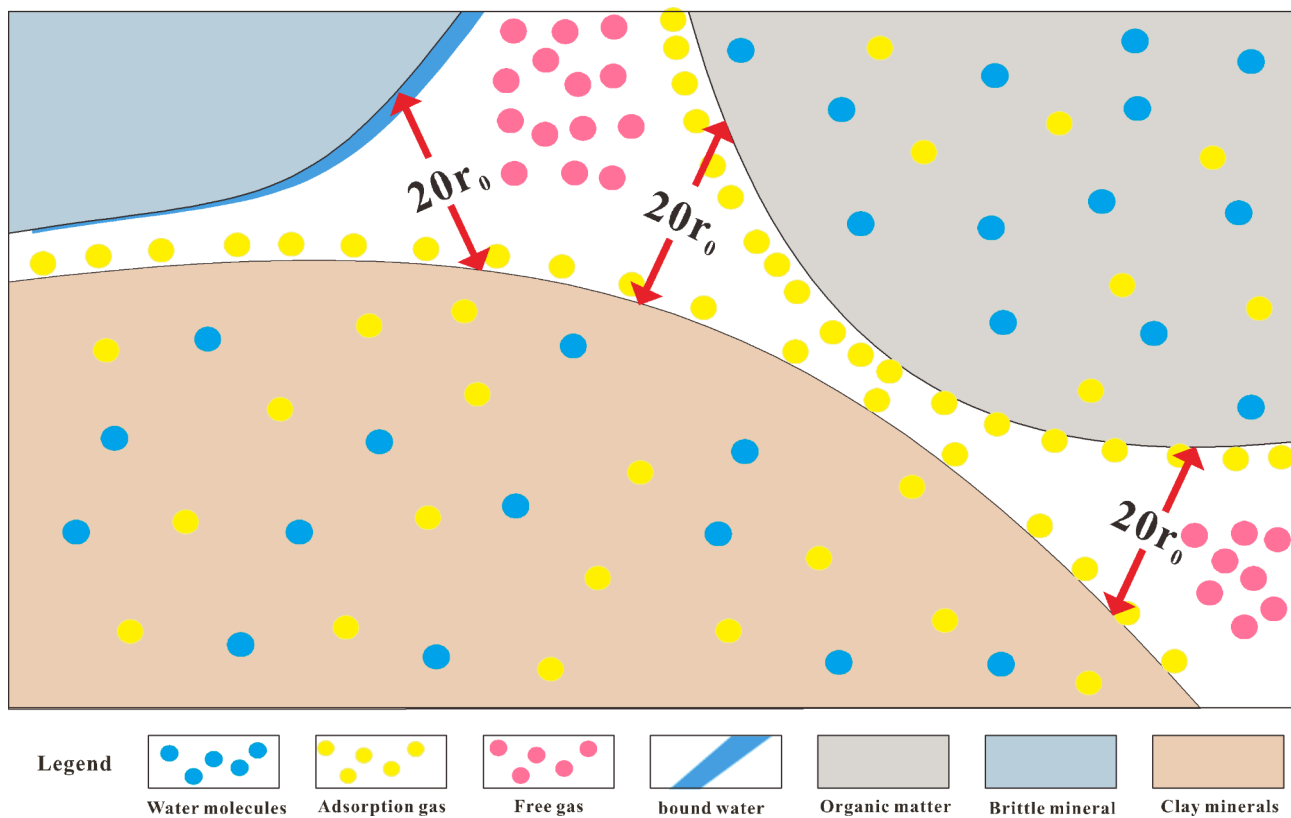


Fig. 5. Schematic diagram of molecule occurrence mechanisms^{48,49}.

Analysis of factors affecting adsorbed gas content

(1) Effect of organic matter on adsorbed gas content.

Organic matter is not only the material source of adsorbed gas, but also the occurrence space of adsorbed gas, and its lipophilicity makes adsorbed methane difficult to escape^{51,52}. Based on the results of the isothermal adsorption experiments in this study, the theoretical maximum value of adsorbed gas content of the shale was calculated, and the correlation between adsorbed gas content and TOC content was analyzed. The results show that adsorbed gas content and TOC content under deep burial conditions have a good positive correlation, with a correlation coefficient of 0.6837 (Fig. 6a).

Different types of kerogens, with noticeable differences in micro-components, vary widely in methane adsorption capacity. The better the type of organic matter is, the stronger the methane adsorption capacity of the organic matter is. Results of previous quantitative studies on the relationship between methane adsorption capacity of different types of shale and types of organic matter showed that the shale with type III kerogen had the strongest capacity of methane adsorption (between 0.40 and 8.19 m³/t, on average 3.51 m³/t), shales with Type I kerogen (between 0.44 and 5.86 m³/t, on average 2.95 m³/t) and Type II kerogen (between 0.57 and 4.24 m³/t, on average of 2.29 m³/t) had similar capacity of methane adsorption (Fig. 6b). The shales in the study area contains mainly type I kerogen, with strong hydrocarbon generation capability. In the thermal evolution stage, associated with the generation and expulsion of hydrocarbons, type I kerogen would generate more organic matter pores, making the specific surface area of organic matter pores and thus the adsorption capacity of shale increase^{52,53}.

With the rise of organic matter maturity, organic pores, especially micropores and mesopores would be created, improving the methane adsorption capability of the shale⁵⁴. But when the maturity of organic matter exceeds a certain point, the pore connectivity would decrease as the oil and solid bitumen formed in the early stage occupy the organic pores, consequently the methane adsorption capacity of the shale would decrease instead of increase. Tang et al. found that the methane adsorption capacity of over-mature shale ($Ro > 2.0\%$) was larger than that of high-mature shale ($1.3\% < Ro < 2.0\%$) for shales with the same abundance and type of organic matter⁵⁵. In this study, the data of Ro and unit adsorbed gas content of different strata in Sichuan Basin and Xiuwu Basin of Jiangxi province were collected. Through analysis, it is found that at the Ro of less than 3%, the adsorbed gas content of shale increases with the increase of Ro; at Ro of 3%, it reaches the maximum; at Ro greater than 3%, it decreases with the increase of Ro (Fig. 6c).

(2) Influence of clay minerals on adsorbed gas content.

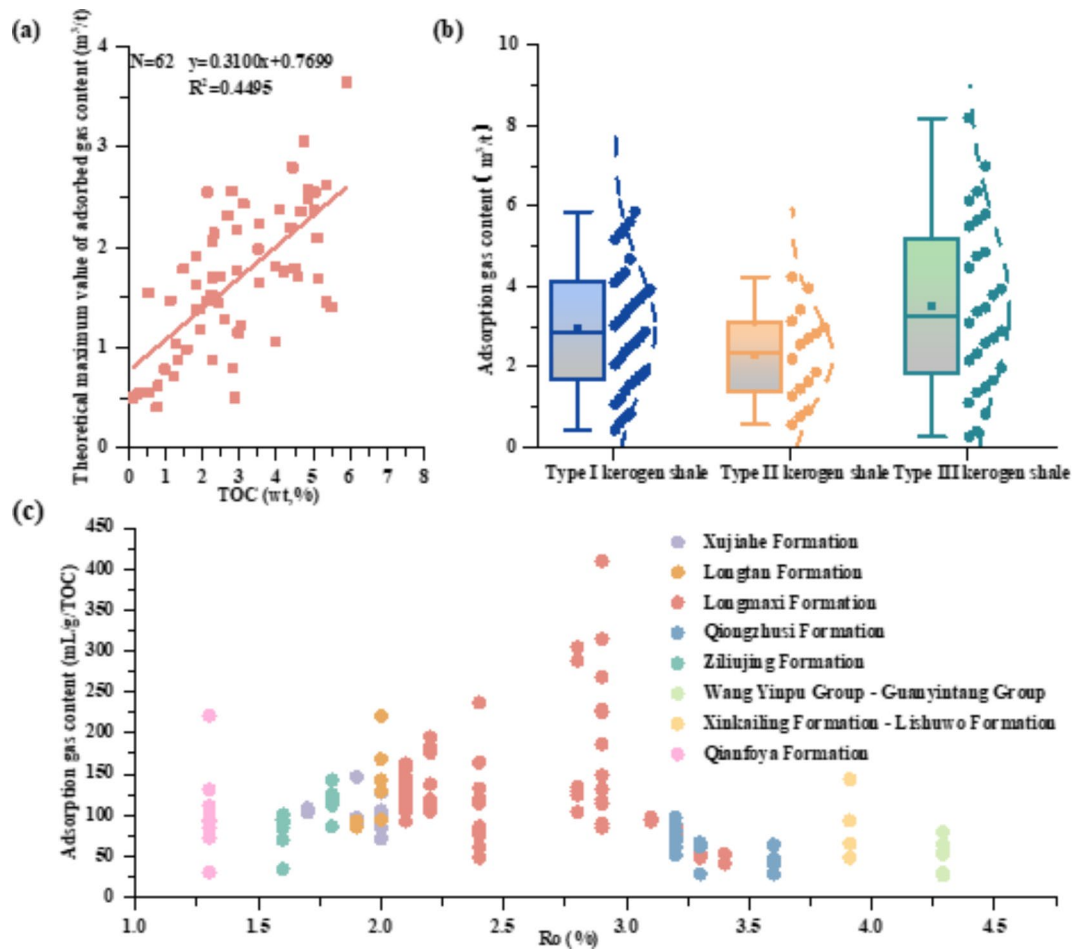


Fig. 6. (a) Relationship between theoretical maximum value of adsorbed gas content and TOC; (b) Relationship between adsorbed gas content and kerogen type; (c) Relationships between adsorbed gas content per unit TOC and maturity of different types of shales.

Different clay minerals in shale have different chemical properties, pore structures and contents, and thus different contributions to shale adsorption capacity, which leads to the complex relationship between shale adsorption capacity and clay mineral content. At present, researchers at home and abroad have wide division on the adsorption capacities of clay minerals. Through the study of Mississippi shales in the United States, Ross and Bustin concluded that the adsorption capacities of clay minerals corresponded to their specific surface areas under anhydrous conditions, illite had the strongest adsorption capacity, montmorillonite came the second, and kaolinite was the last⁵⁴. Through methane isothermal adsorption experiments on anhydrous samples of five clay minerals at 65 °C; Ji et al. reckoned that the adsorption capacities of the five clay minerals in descending order were montmorillonite, illite-montmorillonite mixed layer, kaolinite, chlorite and illite⁸. Based on the assay results of whole rock mineral composition, the correlation between the contents of adsorbed gas and the contents of clay minerals of shale samples from the first sub-Mbr was analyzed in this work, and the results show that there is a good negative correlation between the content of adsorbed gas and content of clay minerals of the shale samples in the study area, with a correlation coefficient of 0.5484 (Fig. 7a). On the one hand, this is because the organic matter in the shale of the study area mostly comes from diatoms^{56–58}, therefore, there is a positive correlation between TOC content and siliceous mineral content, while the shale in the Long₁ sub-member is mainly composed of siliceous minerals, and the proportion of siliceous minerals is inversely proportional to that of clay minerals. Therefore, there is a negative correlation between TOC content and clay mineral content. Organic matter is the main storage space for adsorbed gas, so TOC is positively correlated with adsorbed gas content, while content of clay minerals is negatively correlated with adsorbed gas content. On the other hand, organic matter is lipophilic, so the organic matter at high content will preferentially adsorb methane, while clay minerals are hydrophilic, the presence of formation water will occupy some adsorption sites, greatly reducing the methane adsorption ability of clay minerals.

(3) Effect of water saturation on adsorbed gas content.

The water saturation of shale has a significant effect on its methane adsorption capacity. Water molecules occupy some of the adsorption sites on the pore surface, impairing the adherence of methane to the pore surface;

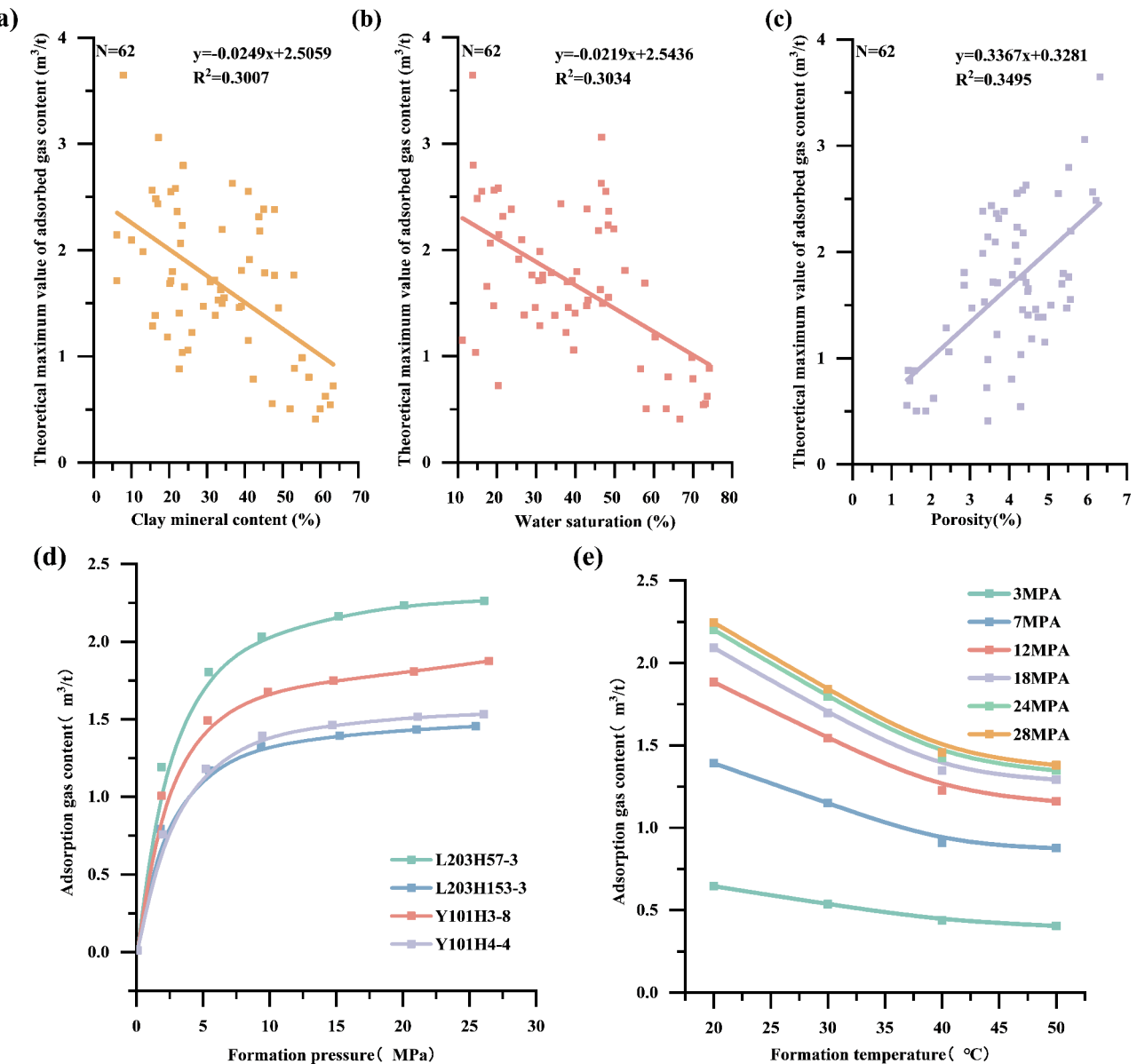


Fig. 7. (a) Relationship between theoretical maximum value of adsorbed gas content and clay mineral content of shale; (b) Relationship between theoretical maximum value of adsorbed gas content and water saturation of the first sub-Mbr shale; (c) Relationship between theoretical maximum value of adsorbed gas content and porosity of the first sub-Mbr shale; and (d) Relationship between adsorbed gas content and formation pressure of the first sub-Mbr shale. (e) Relationship between content of adsorbed gas and formation temperature of the first sub-Mbr shale.

moreover, after water absorption and wetting, clay minerals drop in lipophilicity and thus in adsorption capacity to methane. According to the results of physical property tests, the correlation between the contents of adsorbed gas and water saturations of the shale samples from the first sub-Mbr was analyzed. The results show that there is a good negative correlation between the contents of adsorbed gas and water saturations of the shale samples in the study area, with a correlation coefficient of 0.5484 (Fig. 7b).

(4) Effect of porosity on adsorbed gas content.

Adsorbed gas in shale is adsorbed on the surface of pores, in other words, the content of adsorbed gas depends on pore specific surface area; and the larger the porosity is, the larger the pore specific surface area is^{59–61}. Based on the results of physical property tests, the correlation between the contents of adsorbed gas and porosities of the shale samples from the first sub-Mbr was analyzed, and the results show that there is a good positive correlation between the contents of adsorbed gas and porosities of the shale samples from the study area, with a correlation coefficient of 0.5484 (Fig. 7c).

(5) Effect of formation temperature and pressure on the content of adsorbed gas.

The adsorption capacity of shale is not only affected by the surface properties of the shale itself, but also by the formation temperature and pressure. The experiment under the same TOC content and temperature in this study shows the adsorbed gas content of shale change significantly with the increase of pressure: in the initial stage (from 0 to 5 MPa), the increase of pressure had the most significant effect on the adsorbed gas content, resulting in larger slope of the curve, and then increase in the adsorbed gas content became slower with the further increase in pressure; after the pressure reached 10 MPa, the effect of further pressure increase on the content of adsorbed gas significantly diminished, the content of adsorbed gas basically kept constant, and the control effect of pressure on the content of adsorbed gas gradually decreased (Fig. 7d). Results of the experiment under the same TOC and pressure conditions show with the increase of temperature, the content of adsorbed gas shows a downward trend: when the temperature increased from 20 to 40 °C, adsorption capacity of the shale dropped at a faster rate, and when the temperature exceeded the critical temperature of 40 °C, the decrease rate gradually slowed down (Fig. 7e).

Analysis of factors influencing free gas content

(1) Effect of water saturation on free gas content.

According to the results of physical property tests, the correlation between water saturations and free gas contents of the shale samples from the study area was analyzed. The results shows that the theoretical minimum value of free gas content has a negative linear correlation with water saturation (with a correlation coefficient R of 0.6037) (Fig. 8a), and the free gas content of shale decreases with the increase of water saturation. With the increase of water saturation, water molecules occupy part of the pore volume of shale, resulting in the decrease of occurrence space for free gas and thus the decrease of free gas content, in other words, water saturation has a significant inhibitory effect on free gas content.

(2) Effect of porosity on free gas content.

Pores in shale are the main space holding free methane^{8,22}. There is a positive linear correlation between the theoretical maximum values of free gas content and porosities of shale samples from the study area (with a correlation coefficient R of 0.7448), in other words, the free gas content increases with the increase of porosity, indicating that porosity has a strong control on the free gas content (Fig. 8b).

(3) Influence of formation temperature and pressure on free gas content.

The influence of formation temperature and pressure on the free gas content of shale conforms to Boyle's law. Under the same pressure, with the rise of temperature, the gas volume expands, and the free gas stored in the same space decreases; under the same temperature, with the rise of pressure, the gas volume is compressed, so more free gas can be stored in the same storage space. Clearly, there is a negative linear correlation between the theoretical minimum free gas content and formation temperature (with a correlation coefficient R of 0.7566), indicating that the free gas content decreases with the increase of formation temperature (Fig. 8c). On the contrary, there is a positive linear correlation between the theoretical minimum free gas content and the formation pressure (with a correlation coefficient R of 0.7516), suggesting that the free gas content increases with the increase of formation pressure (Fig. 8d). The formation temperature and pressure both have strong impact on the free gas content of shale.

Quantitative prediction of shale gas content

Quantitative prediction of adsorbed gas content

Isothermal adsorption is a powerful method to describe the gas-bearing characteristic and gas storage capacity of shale, and the Langmuir volume and Langmuir pressure data of each shale sample can be obtained by this method. The isothermal adsorption equation is as follows:

$$V = \frac{V_L P}{P + P_L} \quad (5)$$

where, V is the maximum adsorption capacity of the sample at formation pressure P, m³/t; P is formation pressure, MPa, $P = 1 \times 9.81 \times H \times$ formation pressure coefficient/1000, H is burial depth, m; V_L is Langmuir volume, m³/t; P_L is Langmuir pressure, MPa.

Methane isothermal adsorption experiments at high temperature and high pressure were carried out on 62 samples from 6 wells, Y101H4-4, Y101H3-8 and L203H57-3 etc. in the study area under the condition of equilibrium water, and then the data of the methane isothermal adsorption experiments were fitted by Langmuir equation. The specific steps were as follows:

(1) Establishment of the Langmuir volume prediction relation. Firstly, the correlations between factors affecting adsorbed gas content such as TOC content, clay mineral content, water saturation and porosity measured by experiments, as well as formation temperature calculated with geothermal gradient, formation pressure calculated with formation pressure coefficient and the corresponding Langmuir volumes were analyzed.

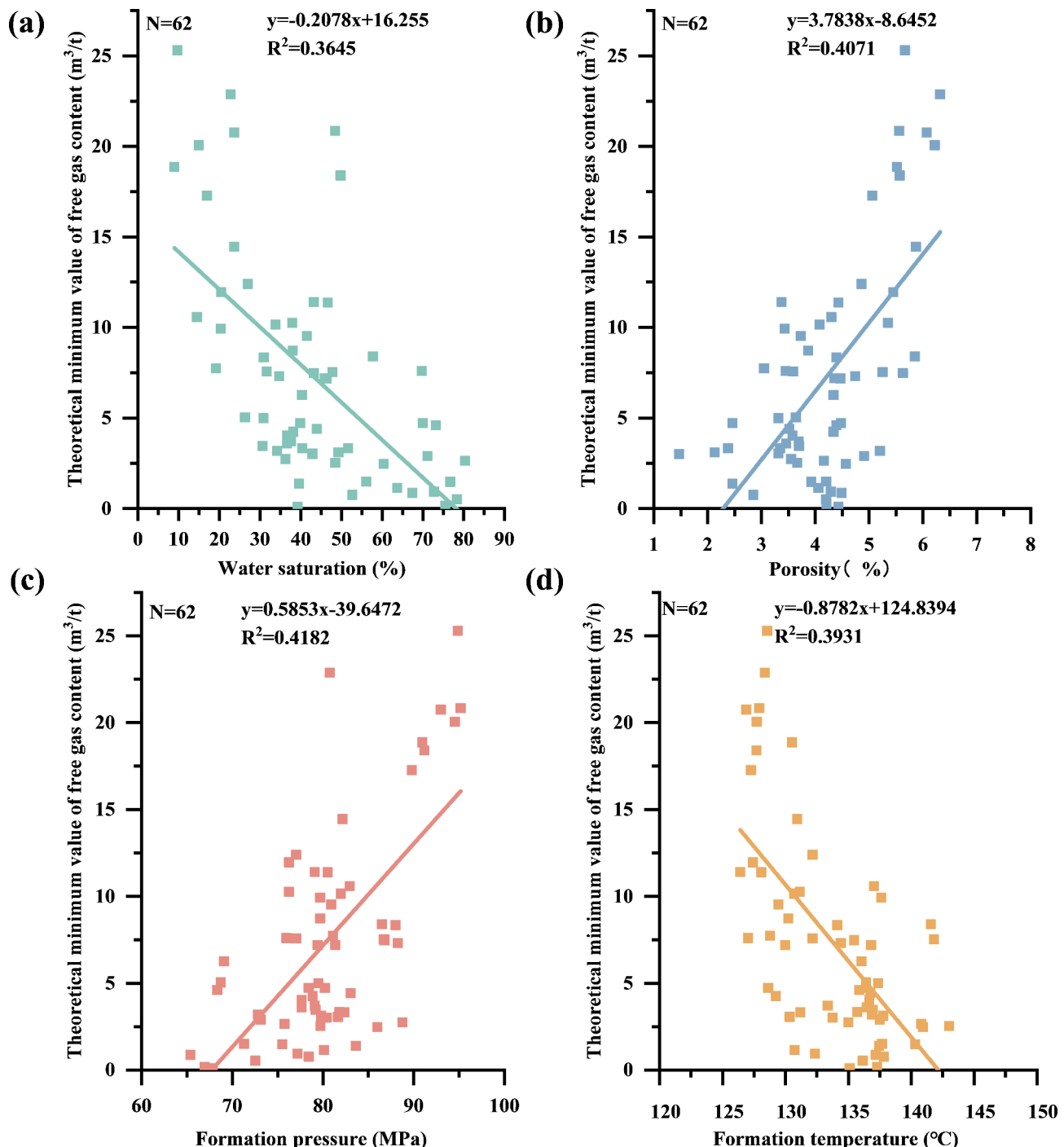


Fig. 8. (a) Relationship between free gas content and water saturation of the first sub-Mbr shale; (b) Relationship between free gas content and porosity of the first sub-Mbr shale; (c) Relationship between free gas content and formation temperature of the first sub-Mbr shale; (d) Relationship between the free gas content and formation pressure of the first sub-Mbr shale.

The results show that Langmuir volume is in positive correlation with TOC content, porosity and formation pressure, with correlation coefficients R of 0.8490 (Fig. 9a), 0.6319 (Fig. 9d) and 0.3763 (Fig. 9f) respectively; and it is in negative correlation with clay mineral content, water saturation and formation temperature, with correlation coefficients R of 0.6459 (Fig. 9b), 0.7053 (Fig. 9c) and 0.6174 (Fig. 9e) respectively. The correlation coefficient R between formation pressure and Langmuir volume is less than 0.5, indicating the correlation is weak, so it was not considered in the fitting. Secondly, the multiple linear regression method was used to derive the relations between Langmuir volume and the main affecting factors.

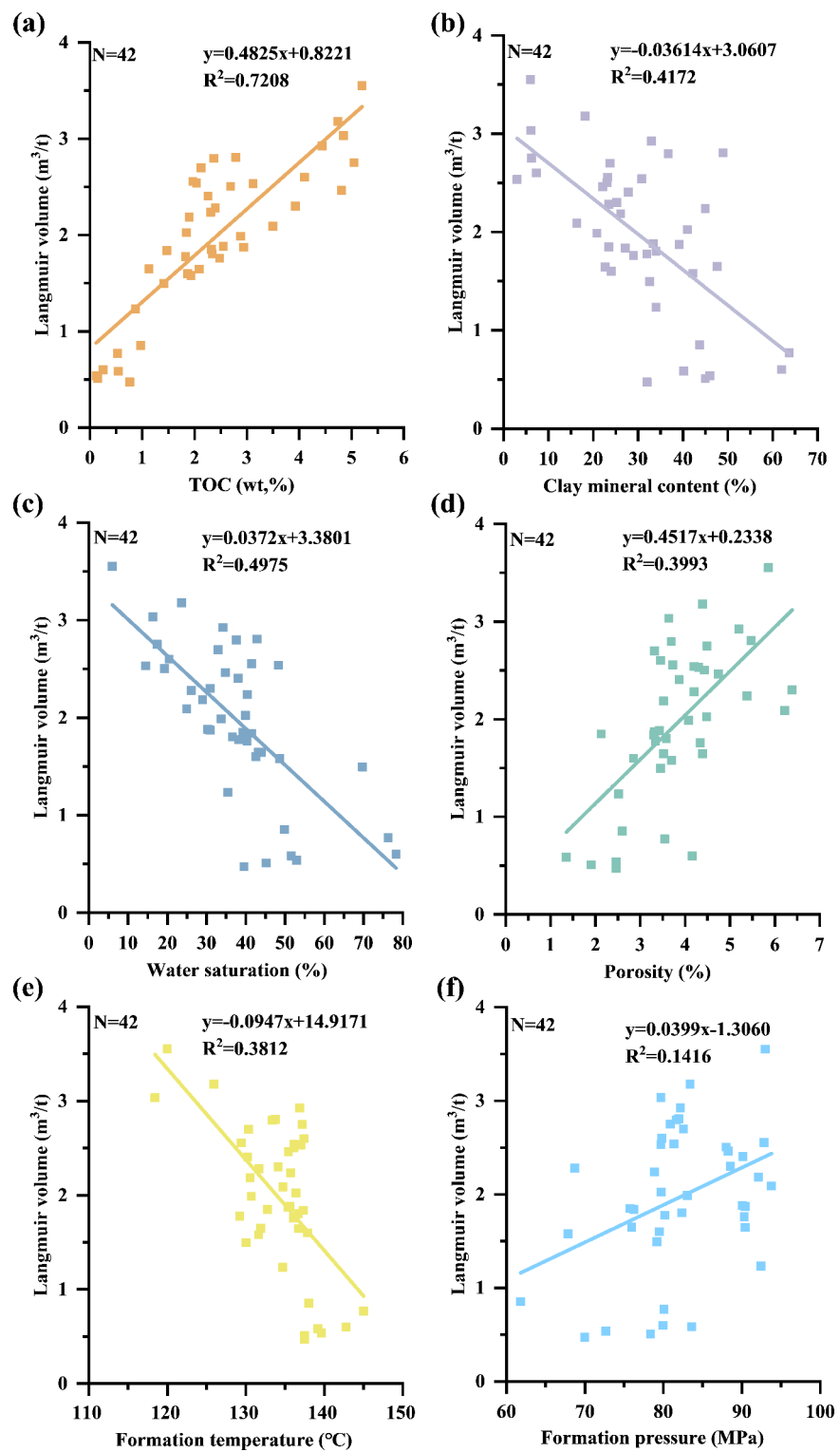


Fig. 9. Relationships between Langmuir volume and the main factors.

Langmuir volume set as the dependent variable, and TOC content, water saturation, porosity, clay minerals and formation temperature assumed as the independent variables, were substituted into the Langmuir volume formula for multiple linear regression fitting to obtain the relations between TOC content, water saturation, porosity, content of clay minerals, formation temperature and Langmuir volume. As shown in Eq. (6):

$$V_L = a \times \text{TOC} + b \times S_w + c \times \phi + d \times T + e \times \text{Clay} + f \quad (6)$$

where a, b, c, d, e and f are the fitting coefficients, dimensionless; V_L is Langmuir volume, m^3/t ; TOC is organic carbon content, %; ϕ is porosity, %; Clay is clay mineral content, %; S_w is water saturation, % and T is formation temperature, $^{\circ}\text{C}$.

By substituting the specific values of independent variables including TOC content, water saturation, porosity, clay mineral content and formation temperature of Luzhou Block into the Eq. (6), specific values of the fitting coefficients, a, b, c, d, e and f, were worked out, as shown in Eq. (7):

$$V_L = 0.434\text{TOC} + 0.034S_w + 0.0133\phi - 0.0112T - 0.002\text{Clay} + 1.596 \quad (7)$$

$$R^2 = 0.9350.$$

(2) Establishment of the Langmuir pressure prediction relation. The relationship between Langmuir pressure and temperature was worked out by linear regression method (Fig. 10), as Eq. (8):

$$\ln(P_L) = \frac{m}{T + 273.15} + n \quad (8)$$

where m, n are the fitting coefficients, dimensionless; P_L is Langmuir pressure, MPa; T is formation temperature, $^{\circ}\text{C}$.

By substituting the specific values of Langmuir pressure and temperature of Luzhou Block into the Eq. (8), the specific values of m and n were calculated, as shown in Eq. (9):

$$\ln(P_L) = \frac{-1232.9049}{T + 273.15} + 4.5120 \quad (9)$$

$$R^2 = 0.9562.$$

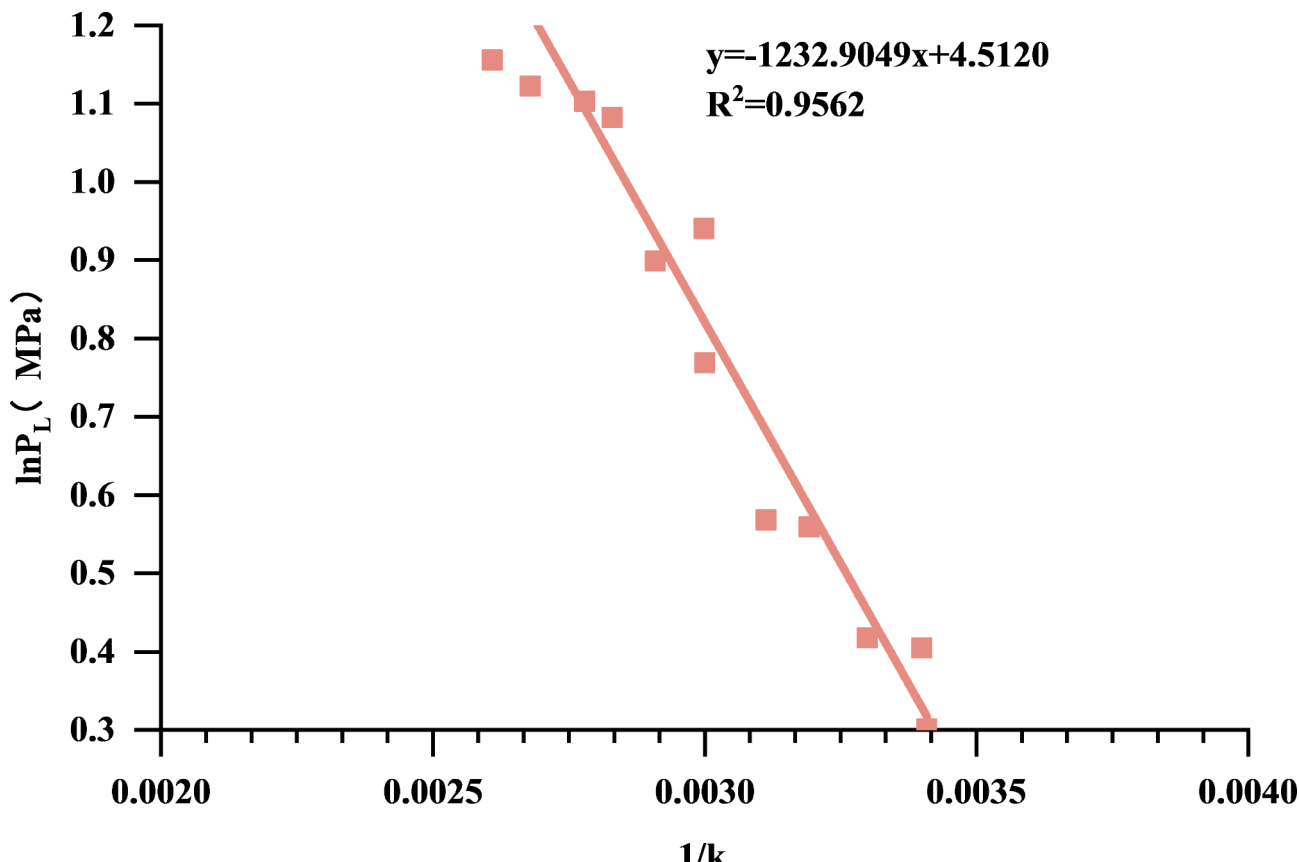


Fig. 10. Langmuir pressure vs. temperature.

(3) Establishment of prediction model of adsorbed gas content. The Langmuir pressure and Langmuir temperature were substituted into the Langmuir equation to obtain an extended Langmuir equation under the joint control of temperature and pressure, i.e., the prediction model of adsorbed gas content, as Eq. (10):

$$V_a = \frac{P \times (a \times TOC + b \times S_w + c \times \phi + d \times T + e \times Clay + f)}{P + e^{(\frac{m}{T+273.15} + n)}} \quad (10)$$

where V_a is the predicted content of adsorbed gas, m^3/t ; TOC is the content of organic carbon, %; ϕ is the porosity, %; Clay is the content of clay minerals, %; S_w is the water saturation, %; T is the formation temperature, $^{\circ}\text{C}$; P is the formation pressure, MPa.

By substituting Eqs. (7) and (9) into the Langmuir equation, the adsorption gas prediction model of Luzhou Block, Eq. (11), was obtained:

$$V_a = \frac{P \times (0.434TOC + 0.034S_w + 0.0133\phi - 0.0112T - 0.002Clay + 1.596)}{P + e^{(\frac{-1232.9049}{T+273.15} + 4.5120)}} \quad (11)$$

The TOC content (TOC), water saturation (S_w), porosity (ϕ), clay mineral content (Clay), formation temperature (T) and formation pressure (P) in Eq. (10) are different for different blocks and target formations in question, resulting in differences in the fitting coefficients in the equation, but the essence of the equation is the same. When the equation (model) is applied to a new block, the specific values of the fitting coefficients in it can be calculated through multiple linear regression by substituting the experimental data of the geological variables of the new block into the equation, and hence the adsorbed gas prediction model suitable for the new block can be worked out.

The established quantitative prediction model of adsorbed gas content was used to reconstruct the characteristics of methane adsorption capacity of shales with different TOC contents in Luzhou Block with the variations of formation burial depth^{63,64}. When the burial depth is shallow (< 1000 m), the pressure is the dominant factor affecting methane adsorption capacity of shale, and the adsorbed gas content increases with the increase of burial depth. When the burial depth is deep (> 1000 m), the temperature becomes the dominant factor affecting methane adsorption capacity of shale, and the adsorbed gas content decreases with the increase of burial depth. At the same TOC content, as temperature and pressure increase with the increase of burial depth, the temperature and pressure affect the adsorbed gas content jointly, so the methane adsorption capacity of the shale increases rapidly at first and then decreases slowly, reaching the maximum at about 750–1000 m. With the increase of TOC content, the adsorbed gas content increases, and the depth at which the shale reaches the maximum adsorption capacity also increases (Fig. 11). On the one hand, shale gas is formed by the thermal evolution of organic matter, so the higher the TOC content, the more shale gas will be generated; on the other hand, the storage space of adsorbed gas is mainly provided by the pore specific surface area, and the pore specific surface area in the study area is mainly provided by organic matter. When the TOC content of shale is 1%, the shale has a maximum methane adsorption of 2.8 m^3/t , when the TOC content of shale is 3%, the shale has a maximum methane adsorption of 3.6 m^3/t , and when the TOC content is 5%, the shale has a maximum methane adsorption of 4.5 m^3/t . The maximum methane adsorption of shale increases by about 0.425 m^3/t for each 1% increase of TOC.

Quantitative prediction of free gas content

Free natural gas mainly exists in pores and fractures of large volumes. Based on actual data, the actual gas equation of state was taken to predict the content of free gas.

(1) The total pore volume of shale includes three parts: the pore volume occupied by adsorbed gas, that occupied by free gas and that occupied by water. According to this relationship, the following Eq. (12) can be obtained:

$$V_{fp} = V_{tp} - V_{ap} - V_{wp} \quad (12)$$

where V_{fp} is the pore volume occupied by free gas, ml/g ; V_{tp} is the total pore volume of shale, ml/g ; V_{ap} is the pore volume occupied by adsorbed gas, ml/g ; V_{wp} is the pore volume occupied by water, ml/g .

(2) The total pore volume of shale was calculated by using porosity and density of the shale:

$$V_{tp} = \frac{\phi}{\rho_r} \quad (13)$$

where V_{tp} is the total pore volume of the shale, m^3/t ; ρ_r is the density of the shale, g/cm^3 ; ϕ is the porosity of the shale, %.

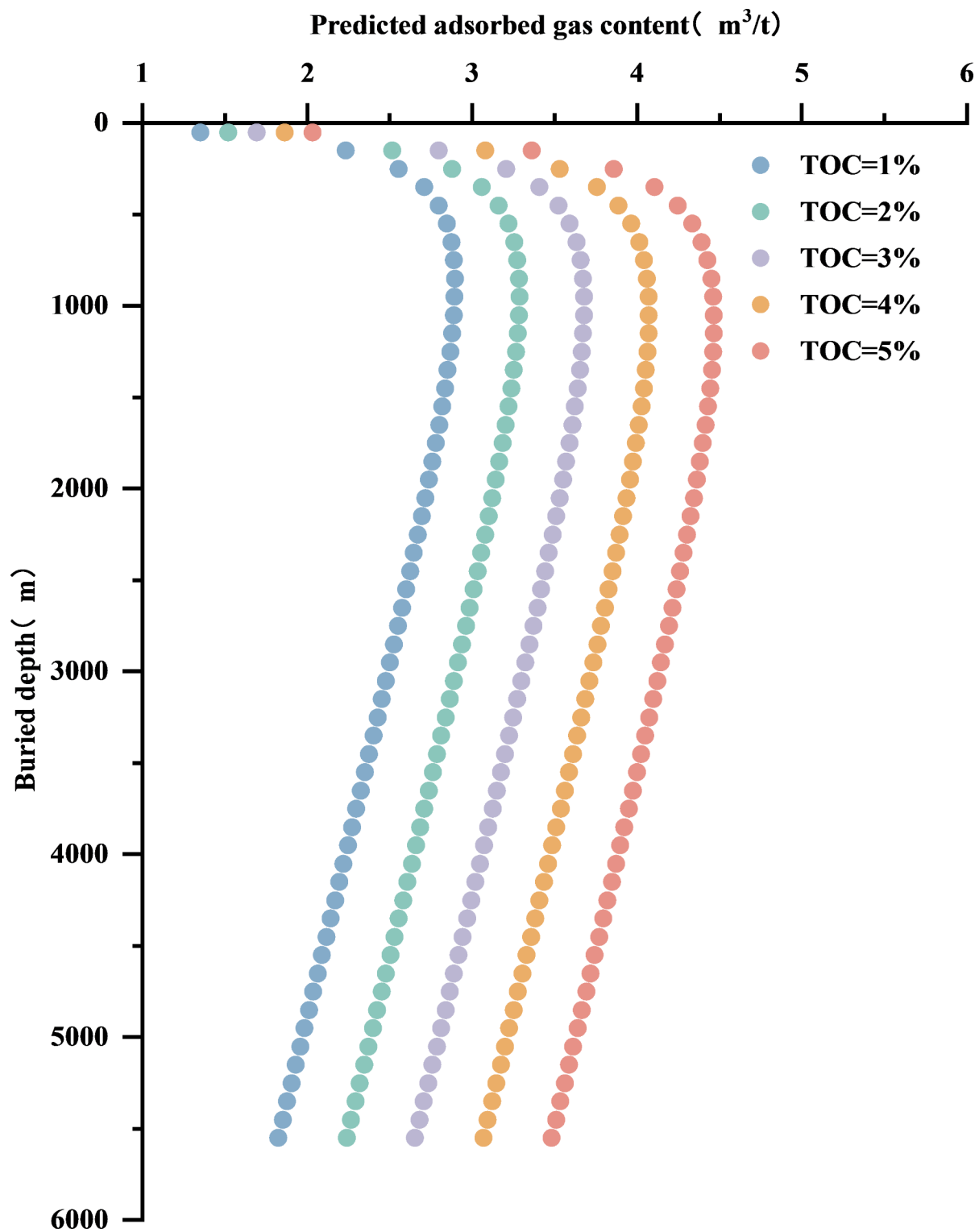


Fig. 11. Curves of adsorbed gas content with burial depth of shales with different TOCs in Luzhou Block.

(3) The pore volume occupied by adsorbed gas was worked out by the equations below:

$$V_{ap} = \frac{n_a \times M}{\rho_a} \quad (14)$$

$$n_a = \frac{P_0 \times V_{a0}}{z_0 \times R \times T_0} \quad (15)$$

where n_a is the amount of adsorbed gas, mol; ρ_a is the density of the adsorbed phase, 0.354 g/cm^3 ; M is the molar mass of the gas, 16 g/mol ; V_{a0} is the absolute adsorption capacity, m^3/t ; P_0 (MPa) and T_0 (K) correspond to the pressure of 0.101 MPa and the temperature of 273.15 K under standard conditions; R is the gas constant, $8.314 \times 10^{-3} \text{ kJ/(mol-K)}$; Z_0 is the compressibility factor of methane under standard conditions, 0.99761 .

(4) The pore volume occupied by water was calculated by the following equation:

$$V_{wp} = \frac{S_w \times V_{tp} \times \rho_{w0}}{\rho_w} = \frac{S_w \times \frac{\phi}{\rho_r} \times \rho_{w0}}{\rho_w} \quad (16)$$

where S_w is water saturation, %; V_{tp} is the total pore volume of shale, m^3/t ; ρ_{w0} is the density of water under standard condition, g/cm^3 ; ρ_w is the density of adsorbed water, 1.5401 g/cm^3 .

Free gas content of shale is related to the density of gas, and the density of gas is controlled by temperature and pressure jointly. Therefore, the prediction model of free gas content was deduced as follows:

$$V_f = \frac{V_{fp} \times \rho_f}{\rho_s} \quad (17)$$

where V_f is the volume of free gas under standard conditions, m^3/t ; V_{fp} is the pore volume occupied by free gas, m^3/t ; ρ_f is the density of free gas in the pore, g/cm^3 ; ρ_s is the density of methane under standard conditions, 0.00071 g/cm^3 .

(5) The prediction model of free gas content was obtained from the above equation:

$$V_f = \frac{\left(\frac{\phi}{\rho_r} - \frac{P_0 \times V_{a0} \times M}{z_0 \times R \times T_0 \times \rho_a} - \frac{S_w \times \frac{\phi}{\rho_r} \times \rho_{w0}}{\rho_w} \right) \times \rho_f}{\rho_{fs}} \quad (18)$$

where V_f is the volume of free gas under standard conditions, m^3/t ; ρ_r is density of the shale, g/cm^3 ; ϕ is porosity, %; P_0 and T_0 correspond to the pressure of 0.101 MPa and the temperature of 273.15 K under standard conditions; R is the gas constant, $8.314 \times 10^{-3} \text{ kJ/(mol-K)}$; Z_0 is the compressibility factor of methane under standard conditions, 0.99761 ; M is the corresponding molar mass of methane, 16 g/mol ; V_{a0} is the absolute adsorption capacity, m^3/t ; S_w is water saturation, %; ρ_{w0} is the density of water under standard conditions, g/cm^3 ; ρ_w is the density of adsorbed water, g/cm^3 ; ρ_f is the density of free gas in the pores, g/m^3 ; ρ_{fs} is the density of methane under standard conditions, 0.00071 g/cm^3 .

At last, the final free gas prediction model was obtained by substituting the constants into Eq. (18):

$$V_f = \left(\frac{1 - 0.0649 \times S_w \times \phi}{0.00071 \times \rho_r} - 0.0021 \times V_{a0} \right) \times \rho_f \quad (19)$$

where S_w is water saturation, %; ϕ is porosity of the shale, %; ρ_r is density of the shale, g/cm^3 ; V_{a0} is the absolute adsorption capacity obtained by the adsorbed gas prediction model, m^3/t ; ρ_f is the density of free gas in the pores, g/cm^3 .

Equation (19) is transformed from the actual gas equation of state, in which the parameters such as water saturation (S_w), porosity (ϕ), absolute adsorption (V_{a0}), shale density (ρ_r) and density of free gas in pores (ρ_f) vary with different study blocks, but the equation doesn't change with the change of the study blocks as there aren't unknown fitting coefficients in it. In other words, it applies to various blocks.

According to the free gas prediction model, the variation patterns of free gas storage capacity of shale layers with different porosities and water saturations with formation burial depth in Luzhou block were reconstructed. As free gas content is mainly controlled by porosity, water saturation, formation temperature and pressure. At

the same TOC, with the increase of depth, the shale layer increases in temperature and pressure constantly, under the joint effect of temperature and pressure, gas content of the shale increases with the increase of depth, because under burial conditions of deep layers, compared with temperature, pressure has a stronger control on free gas, with the increase of burial depth, formation pressure increases, gas is compressed, so more free gas can be stored in the same space. At the same burial depth, the content of free gas increases with the increase of porosity, specifically by $1.37 \text{ m}^3/\text{t}$ for each 10% increase of porosity. In contrast, with the increase of water saturation, the free gas content decreases, specifically, by $0.51 \text{ m}^3/\text{t}$ for each 10% increase of water saturation. The porosity has a more significant effect on free gas content, about 2.7 times that of water saturation (Fig. 12).

Validation and application of the model

As shown in Figs. 13 and 14, the analysis data of core samples from Well Y101H10-3 (at buried depths of 3743.8–3884.78 m) and Well L211 (at buried depths of 4851.63–4929.62 m) were substituted into the model proposed in this paper, and the adsorbed gas volume, free gas content and total gas content of these two wells at different depths were calculated. For Well Y101H10-3 (at buried depths of 3743.8–3884.78 m), the predicted average adsorbed gas content was $3.28 \text{ cm}^3/\text{g}$, accounting for 30% of the total gas content, and the predicted average free gas content was $5.27 \text{ cm}^3/\text{g}$, accounting for 70% of the total gas content. The predicted average content of adsorbed gas in Well L211 (at buried depths from 4851.63 to 4929.62 m) was $2.72 \text{ cm}^3/\text{g}$, accounting for 38% of the total gas content, and the predicted average content of free gas was $6.20 \text{ cm}^3/\text{g}$, accounting for 62% of the total gas content. Therefore, it is inferred that with the increase of buried depth, the total gas content increases and the proportion of free gas increases too. It can be seen from the correlation (Fig. 15) between the predicted gas contents of Well Y101H10-3 and Well L211 and the measured gas contents of core samples that, although some individual points had large differences from the measured data, the correlation coefficient between the predicted gas contents and the measured gas contents can reach more than 0.88, indicating the results of the model can meet the accuracy required for shale gas content prediction in the study area.

Furthermore, the prediction models proposed in this paper were applied to the whole Luzhou block, and the adsorbed gas volume, free gas content and total gas content of the target layer of each coring well in the block were calculated, and a plane contour chart was drawn. It can be seen from the chart that on the plane, the adsorbed gas is mainly stored in the area around Well L205, Well L203H91-1, Well Y101H10-3, Well Y101H4-4 and Well L210 in the middle of the study area, and the adsorbed gas content gradually decreases to the south and north (Fig. 16a); the free gas mainly accumulates in the area around Well L203, Well L203H91-1, Well L203H153-8 and Well L203 H175-1 in the west of the study area, and the area around Well Y101H75-1, Well L210 and Well Y101H65-5 in the southeast of the study area, and the free gas content drops gradually to the southwest and north (Fig. 16b). According to the total gas content, the study area was divided into Class I, II and III gas-bearing areas. The results show that the Class I gas-bearing area is distributed along Well L205, Well L203H91-1 and Well Y101H75-1, areas outside of which gradually transit to Class II and Class III gas-bearing areas (Fig. 16c). Statistics and comparison of the gas contents and EUR of all the wells show that the higher the gas content of a well, the greater the EUR of the well, and the two have a good correlation, with a correlation coefficient of about 0.90 (Fig. 17).

Conclusions

The important conclusions could be drawn as follows from this study:

- (1) Among the minerals in the shale samples from the first sub-Mbr, siliceous minerals are dominant, with an average content of about 45%, clay minerals take the second place, with an average content of about 33%, carbonate minerals take the third place, with an average content of about 18%, besides, a small amount of pyrite is occasionally seen. The shale samples are in the stage of over-mature and semi-graphitization, contain largely type I organic matter, and have TOCs between 2.91% and 4.48% and abundant organic matter pores.
- (2) The content of adsorbed gas is mainly affected by Ro, TOC content, porosity, water saturation, clay mineral content, formation temperature and pressure. Based on the Langmuir equation, a prediction model of adsorbed gas content under the joint control of multiple factors was established by using the multiple linear regression method and introducing the controlling factors such as TOC content, porosity, water saturation, clay mineral content, formation temperature and pressure etc.
- (3) The content of free gas is mainly controlled by porosity, water saturation, formation temperature and pressure. Based on the extended ideal gas equation of state, the prediction model of free gas content was established by considering the controlling factors such as porosity, water saturation, formation temperature and pressure etc.
- (4) Analysis data of cores taken from different burial depths of two wells were substituted into the models for verification. The results show the correlation coefficient between the predicted gas contents and measured gas contents was more than 0.88, showing good coincidence. According to the prediction models, the adsorbed gas content, free gas content and total gas content of each well were calculated, and the study area was divided into Class I (with a total gas content $\geq 11 \text{ m}^3/\text{t}$), Class II (with a total gas content between $9 \text{ m}^3/\text{t}$ and $11 \text{ m}^3/\text{t}$), and Class III (with a total gas content $< 9 \text{ m}^3/\text{t}$) gas-bearing areas. The Class I gas-bearing area is distributed along Well L205, Well L203H91 and Well Y101H75-1. Predicted gas contents and EUR of all wells in the study area were counted and compared. The results show that the higher the predicted gas content of a well is, the higher the EUR of the well is, and the correlation coefficient between them is about 0.90.

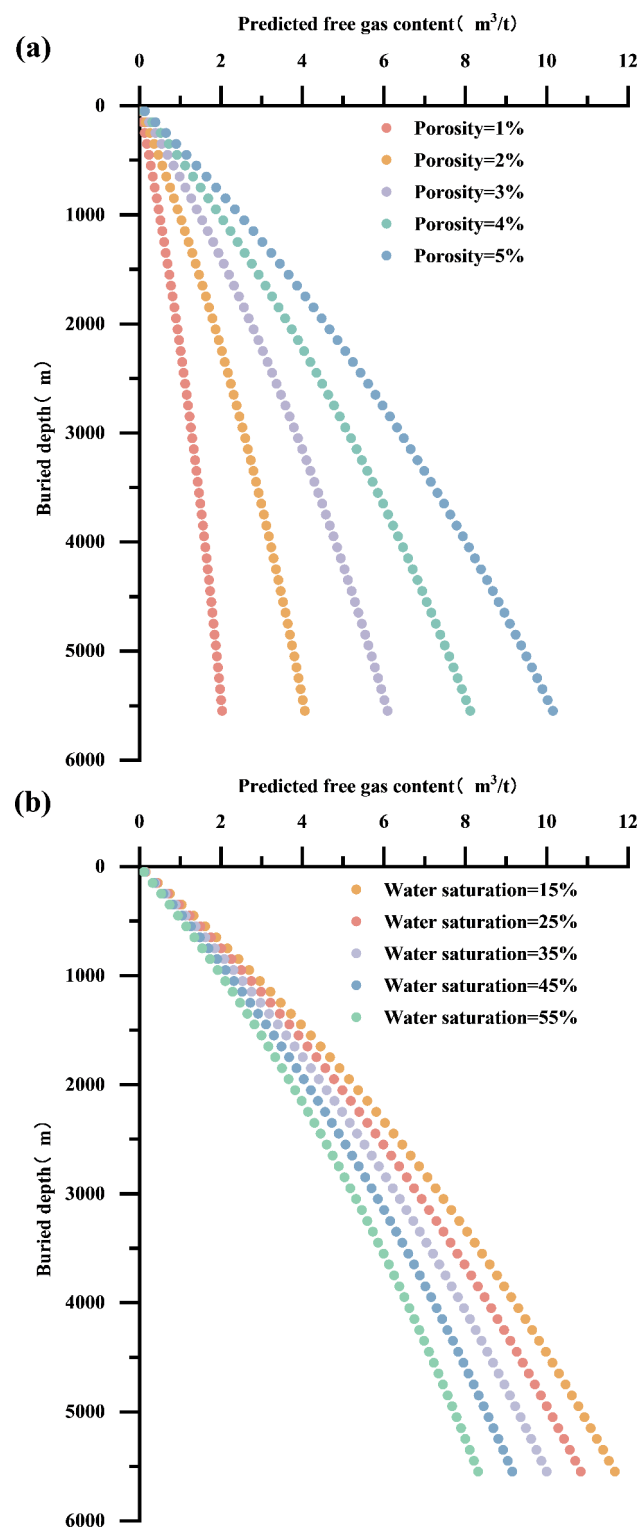


Fig. 12. (a) Curves of free gas content vs. burial depth of shales with different porosities in Luzhou Block; (b) Curves of free gas content vs. burial depth of shales with different water saturations in Luzhou Block.

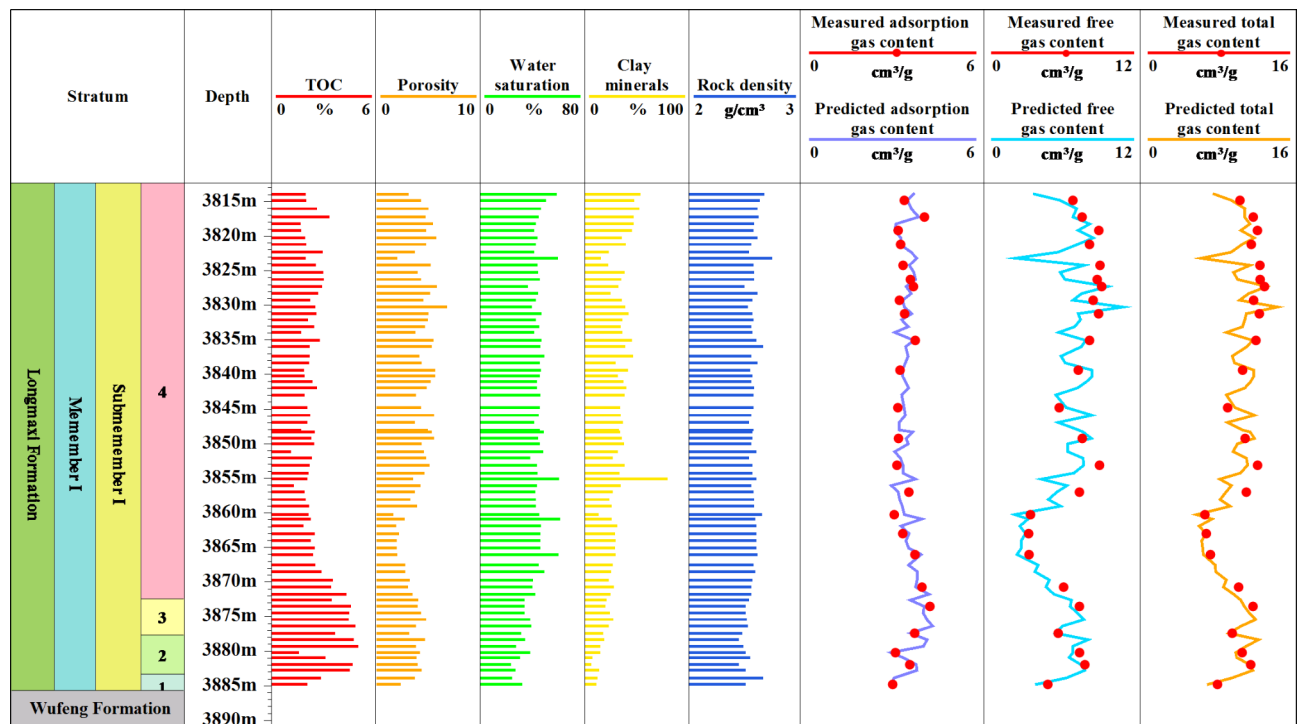


Fig. 13. Predicted gas contents of Long11 in Well Y101H10-3, Luzhou Block.

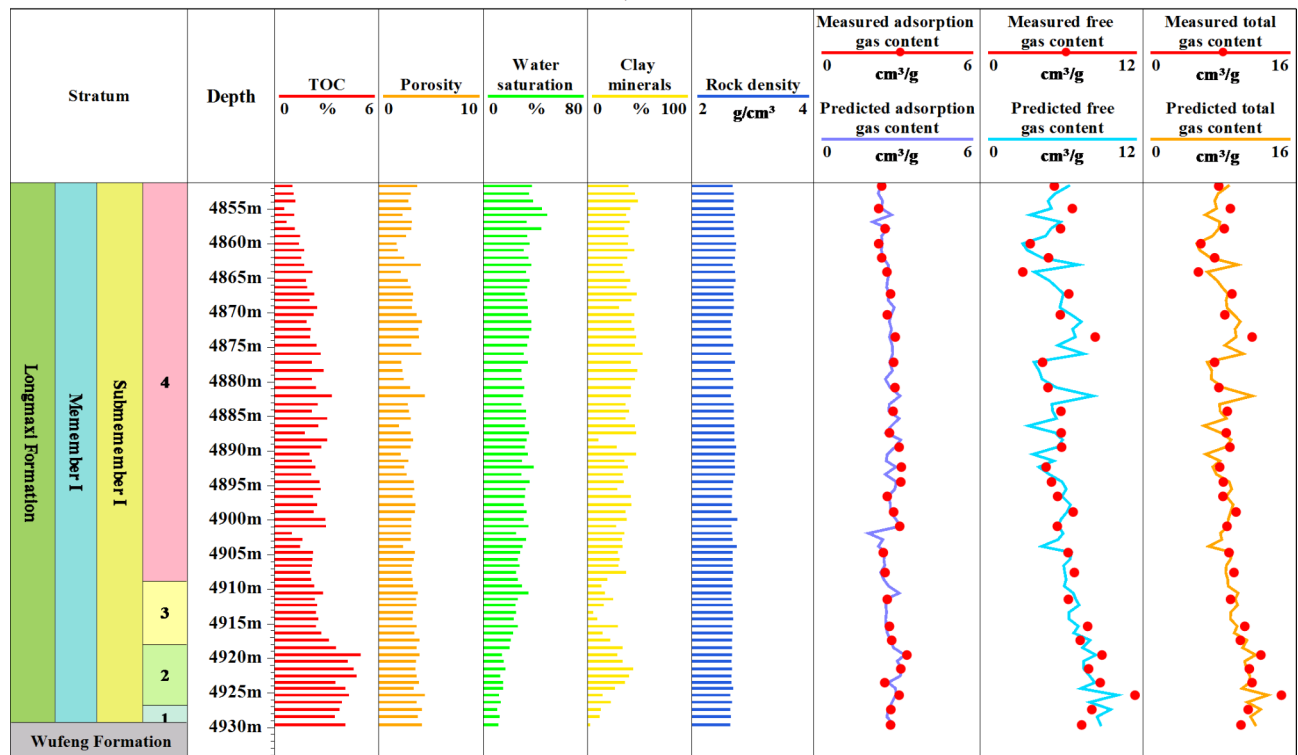


Fig. 14. Predicted gas contents of Long11 in Well L211, Luzhou Block.

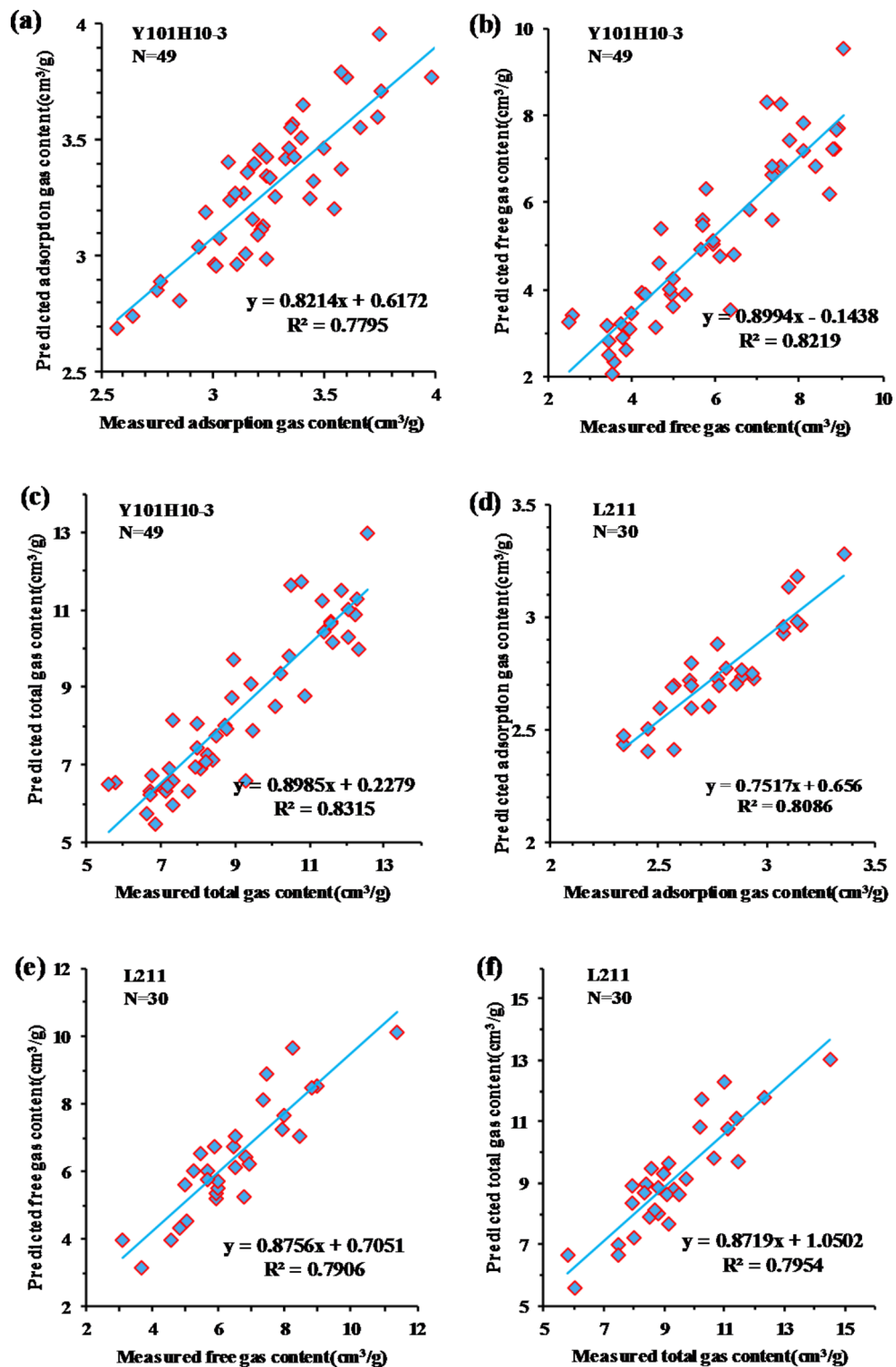


Fig. 15. Correlation analysis of predicted gas contents and measured gas contents.

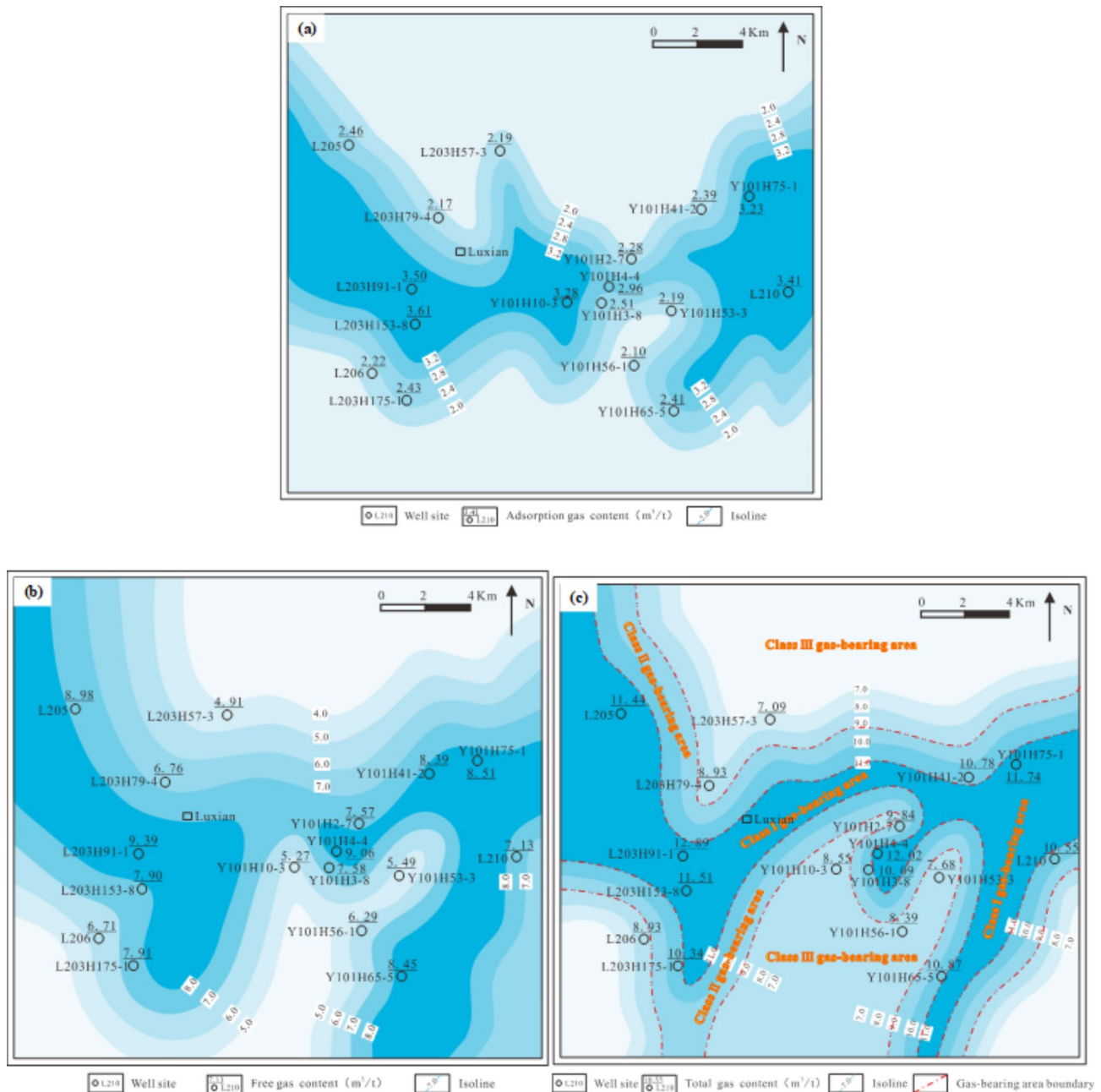


Fig. 16. (a) Contour map of predicted adsorbed gas contents; (b) Contour map of predicted free gas contents; (c) Contour map of predicted total gas contents.

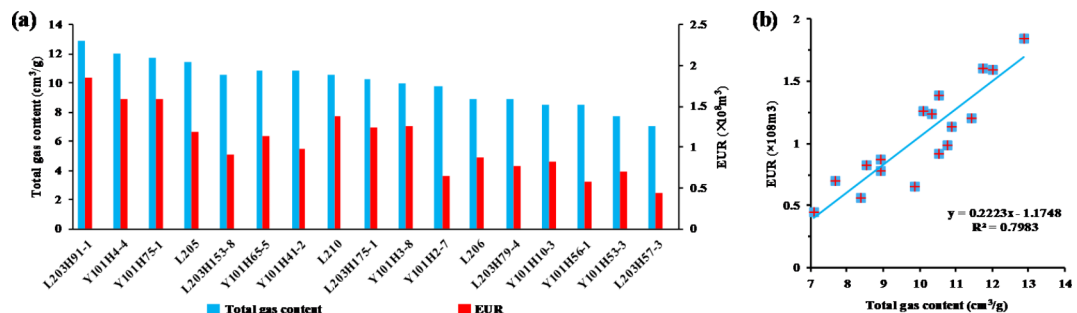


Fig. 17. (a) Predicted total gas contents versus EURs; (b) Correlation analysis between predicted gas contents and EURs.

Data availability

All data generated or analysed during this study are included in this published article.

Received: 18 April 2024; Accepted: 8 January 2025

Published online: 14 January 2025

References

- Guo, X. et al. Discovery and exploration of fuling shale gas field. *China Petroleum Explor.* **21** (3), 24–37 (2016). (in Chinese with English abstract).
- Li, H. et al. Characteristics, formation periods and genetic mechanisms of tectonic fractures in the tight gas sandstones reservoir: a case study of Xujiahe formation in YB area, Sichuan Basin, China. *J. Petrol. Sci. Eng.* **178**, 723–735 (2019). (in Chinese with English abstract).
- Nie, H. et al. Dissolution pore types of the Wufeng Formation and the Longmaxi Formation in the Sichuan Basin, south China: Implications for shale gas enrichment. *Mar. Pet. Geol.* **101**, 243–251 (in Chinese with English abstract).
- Wang, R. et al. Differential characteristics of the upper ordovician-lower silurian Wufeng-Longmaxi shale reservoir and its implications for exploration and development of shale gas in/around the Sichuan Basin. *Acta Geol. Sin. Engl. Ed.* **93**(3), 520–535 (2019). (in Chinese with English abstract).
- Fan, C. et al. Complicated fault characterization and its influence on shale gas preservation in the Southern Margin of the Sichuan Basin, China. *Lithosphere* **2022**(2022(Special 12)), 8035106 (2022). (in Chinese with English abstract).
- Zhu, B. et al. New insights into the evaluation criteria for high-quality deep marine shale gas reservoirs in the Longmaxi formation: evidence from organic matter pore development characteristics. *Front. Ecol. Evol.* **11**. (2023).
- Chalmers, G. R. L. & Bustin, R. M. Lower cretaceous gas shales in northeastern British Columbia, Part I: geological controls on methane sorption capacity. *Bull. Can. Pet. Geol.* **56**(1), 1–21. <https://doi.org/10.2113/gscpgbull.56.1.1> (2008).
- Ji, L. et al. Micro-pore characteristics and methane adsorption properties of common clay minerals by electron microscope scanning. *Acta Pet. Sin.* **33**(02), 249–256 (2012).
- Guo, X. et al. Occurrence mechanism and exploration potential of deep marine shale gas in Sichuan Basin. *Acta Pet. Sin.* **43**(4), 453–468 (2022) (in Chinese with English abstract).
- Gong, Y. et al. Study on the distribution characteristics of occurrence modes of shale gas in the Sichuan Basin and its periphery. *Unconv. Oil Gas.* **10** (2), 49–56 (2023). (in Chinese with English abstract).
- Guo, X. et al. Major factors controlling the accumulation and high productivity in marine shale gas in the lower paleozoic of Sichuan Basin and its periphery: a case study of the Wufeng-Longmaxi formations of Jiaoshiba area. *Geol. China.* **41**(3), 893–901 (2014). (in Chinese with English abstract).
- Wang, Z. et al. The gas-bearing characteristics analysis of the Longtan formation transitional shale in well Xiye 1. *Earth Sci. Front.* **22**(02), 243–250 (2015). (in Chinese with English abstract).
- Zhang, T. et al. Geological control factors of shale gas enrichment in the Wufeng-Longmaxi formation of the Zhaotong National Shale Gas demonstration area. *Nat. Gas. Ind.* **43**(4), 93–102 (2015). (in Chinese with English abstract).
- He, Z. et al. The main factors of shale gas enrichment of Ordovician Wufeng Formation Silurian Longmaxi Formation in the Sichuan Basin and its adjacent areas. *Earth Sci. Front.* **23**(2), 008–017 (2016) (in Chinese with English abstract).
- Li, Q. et al. Dynamic evolution model of shale gas occurrence and quantitative evaluation of gas-bearing capacity. *Geol. Rev.* **66**(02), 457–466 (2020). (in Chinese with English abstract).
- Shan, X. et al. Shale lithofacies and gas-bearing characteristics of the lower paleozoic wufeng formation-member 1 of Longmaxi Formation in Changning Area, Southern Sichuan. *J. Jilin Univ. (Earth Sci. Ed.)* **53**(5), 1323–1337 (2021). (in Chinese with English abstract).
- Wu, W. et al. Gas-in-place content of deep shales and its main controlling factors: a case study on the Wufeng-Longmaxi Shales in the Middle Luzhou Block of the Southern Sichuan Basin, China. *Energy Fuels.* **37** (12), 8296–8310 (2023).
- Xiang, K. et al. Reservoir characteristics and main controlling factors of gas content of deep shale gas in Southern Sichuan Basin. *J. Northeast Pet. Univ.* **47**(3), 44–55 (2023) (in Chinese with English abstract).
- Chen, S. et al. Differences in shale gas accumulation process and its significance in exploration of Lower Silurian Longmaxi formation in Northeast Yunnan. *Front. Earth Sci.* **15**(2), 343–359 (2021).
- Dong, T. et al. Paleodepositional conditions and organic matter accumulation mechanisms in the Upper Ordovician-lower Silurian Wufeng-Longmaxi shales, Middle Yangtze region, South China. *Mar. Pet. Geol.* **143** (2022).
- Huang, Z. et al. *Differential Sedimentary Mechanisms of Upper Ordovician-Lower Silurian Shale in Southern Sichuan Basin, China*, vol. 148 (Marine and Petroleum Geology, 2023).
- Zhang, Z. et al. Control model of organic shale enrichment by terrigenous weathering in Wufeng Formation-Longmaxi Formation, Southeast Sichuan. *China Miner.* **13**(6). (2023).
- Li, Y. et al. Sedimentary facies of marine shale gas formations in Southern China: the Lower Silurian Longmaxi formation in the Southern Sichuan Basin. *J. Earth Sci.* **27** (5), 807–822 (2016).
- Wu, Y. et al. Sedimentary facies of the Longmaxi Formation shale gas reservoir in the Weiyuan area based on elemental characteristics. *Geofluids* **2021**. (2021).

25. Wang, Y. et al. Characteristics and geological significance of organic matter veins in shale reservoir: a case study of the silurian Longmaxi formation in Luzhou area, Sichuan Basin. *Minerals.* **13**(8) (2023).
26. Yan, C. et al. Influence of sedimentary environment on organic matter enrichment in shale: a case study of the Wufeng and Longmaxi formations of the Sichuan Basin, China. *Mar. Pet. Geol.* **92**, 880–894 (2018).
27. Zhao, S. et al. Development of Upwelling during the sedimentary period of the Organic-Rich Shales in the Wufeng and Longmaxi formations of the Upper Yangtze Region and its impact on Organic Matter Enrichment. *J. Mar. Sci. Eng.* **7**(4). (2019).
28. Zeng, C. et al. Distribution characteristics of nanopores and discriminant characteristics of sedimentary environment of the Longmaxi Formation in the Southern Sichuan Basin. *Fresenius Environ. Bull.* **31** (8), 8143–8149 (2022).
29. Guo, W. et al. Characteristics of structural deformation in the southern Sichuan Basin and its relationship with the storage condition of shale gas. *Nat. Gas. Ind.* **41**(05), 11–19 (2021). (in Chinese with English abstract).
30. Chen, L. et al. Tectonic fracture characteristics and formation stages of Longmaxi Formation in Shuanglong-Luochang areas, southern Sichuan Basin. *Nat. Gas Geosci.* **33**(5), 789–798 (2022) (in Chinese with English abstract).
31. Lan, B. F. et al. Investigation of the enrichment and accumulation of normal pressure shale gas in Anchang Syncline outside of Sichuan Basin. *Front. Earth Sci.* **9** (2022).
32. Li, J. et al. *Numerical Simulation of the Palaeotectonic Stress Field and Prediction of the Natural Fracture Distribution in Shale gas Reservoirs: A Case Study in the Longmaxi Formation of the Luzhou area, Southern Sichuan Basin, China* (Geological Journal, 2023).
33. Jiang, S. et al. *Intensive Geological Alteration and gas Accumulation in Longmaxi Formation Shales at Moderate and Great Depths: A Case Study of the Luzhou area in the Southern Sichuan fold zone, China* (Geological Journal, 2023).
34. Zhang, K., Jia, C. Z. & Song, Y. et al., Analysis of Lower Cambrian shale gas composition, source and accumulation pattern in different tectonic backgrounds: A case study of Weiyuan Block in the Upper Yangtze region and Xiuwu Basin in the Lower Yangtze region. *Fuel.* **263** (2020).
35. Zhang, K. et al. Connectivity of organic matter pores in the Lower Silurian Longmaxi Formation shale, Sichuan Basin, Southern China: Analyses from helium ion microscope and focused ion beam scanning electron microscope. *Geol. J.* **57**(5), 1912–1924 (2022).
36. Tang, X. et al. The effect of the variation in material composition on the heterogeneous pore structure of high-maturity shale of the silurian longmaxi formation in the southeastern Sichuan Basin China. *J. Nat. Gas Sci. Eng.* **2015**(23-) (2015).
37. Zhang, Y. et al. Controls on the organic carbon content of the lower Cambrian black shale in the southeastern margin of Upper Yangtze. *Pet. Sci.* **15** (4), 709–721 (2018).
38. Curtis, M. E., Cardott, B. J., Sondergeld, C. H. & Rai, C. S. The development of organic porosity in the woodford shale related to thermal maturity. In *Paper presented at the SPE Annual Technical Conference and Exhibition, San Antonio, Texas, USA, October 2012.* <https://doi.org/10.2118/160158-MS> (2012).
39. Klaver, J., Desbois, G., Urai, J. L. & Littke, R. BIB-SEM study of the pore space morphology in early mature Posidonia Shale from the Hils area, Germany. *Int. J. Coal Geol.* **103**, 12–25 (2012).
40. Zhang, H. et al. SEM observation of organic matters in the Eopaleozoic shale in South China. *Oil Gas Geol.* **36**(04), 675–680 (2015) (in Chinese with English abstract).
41. Karamov, T., Leushina, E., Kozlova, E. & Spasennykh, M. Broad ion beam-scanning electron microscopy characterization of organic porosity evolution during thermal treatment of bazhenov shale sample. *SPE Res. Eval. Eng.* **26**, 64–74 (2023).
42. Hildenbrand, A. et al. Evolution of methane sorption capacity of coal seams as a function of burial history—a case study from the Campine Basin, NE Belgium. *Int. J. Coal Geol.* **66**(3), 179–203 (2006).
43. Gasparik, M. et al. Geological controls on the methane storagecapacity in organic-rich shales. *Int. J. Coal Geol.* **123**, 34–51 (2014).
44. Rexer, T. F. et al. High-pressure methane adsorption and characterization of pores in Posidonia shales and isolated kerogens. *Energy Fuels* **28**(5), 2886–2901 (2014).
45. Ji, L. et al. Experimental investigation of main controls to methane adsorption in clay-rich rocks. *Appl. Geochem.* **27**(12), 2533–2545 (2012).
46. Lennard-Jones, J. E. *Cohes. Proc. Phys. Soc.* **43**(5), 461 (1931).
47. Van der Waals, J. D. *Over de Continuiteit van den Gas-en Vloeistofoestand (On the Continuity of the Gas and Liquid State)*. Ph.D. Thesis, University of Leiden, Leiden (1873).
48. Ji, W. et al. Geological controls and estimation algorithms of lacustrine shale gas adsorption capacity: a case study of the triassic strata in the southeastern Ordos Basin, China. *Int. J. Coal Geol.* **134**, 61–73 (2014).
49. Ji, W. et al. Estimation of marine shale methane adsorption capacity based on experimental investigations of Lower Silurian Longmaxi formation in the Upper Yangtze Platform, south China. *Mar. Pet. Geol.* **68**, 94–106 (2015).
50. Fu, X. & Wang, Z. Dissolution mechanism and solubility equation of gas in water. *Sci. China Ser. B.* **26** (2), 124–130 (1996). (in Chinese with English abstract).
51. Jarvie, D. M., Hill, R. J. & Ruble, T. E. Unconventional shale-gas systems: The Mississippian Barnett Shale of north-central Texas as one model for thermogenic shale-gas assessment. *AAPG Bull.* **2007**(4), 91 (2007).
52. Chalmers, G. R. L., Ross, D. J. K. & Bustin, R. M. Geological controls on matrix permeability of Devonian Gas Shales in the Horn River and Liard basins, northeastern British Columbia, Canada. *Int. J. Coal Geol.* **103** (2012).
53. Bustin, R. M. & Clarkson, C. R. Geological controls on coalbed methane reservoir capacity and gas content. *Int. J. Coal Geol.* **38**(66), 3–26 (1998).
54. Ross, D. J. K. & Bustin, R. M. The importance of shale composition and pore structure upon gas storage potential of shale gas reservoirs. *Mar. Pet. Geol.* **26**(6), 916927 (2009).
55. Tang, S. & Fan, E. Methane adsorption characteristics of clay minerals in organic-rich shales. *J. China Coal Soc.* **39**(8), 1700–1706 (2014) (in Chinese with English abstract).
56. Wang, S. et al. Biogenic silica of organic-rich shale in Sichuan Basin and Its significance for shale gas. *Acta Scientiarum Naturalium Universitatis Pekinensis.* **50**(03), 476–486 (2014).
57. Liu, G. et al. Quartz crystallinity index: New quantitative evidence for biogenic silica of the late ordovician to early silurian organic-rich shale in the Sichuan Basin and adjacent areas, China. *Sci. China Earth Sci.* **64** (5), 773–787 (2021). (in Chinese with English abstract).
58. Zhang, K. et al. Formation mechanism of the sealing capacity of the roof and floor strata of marine organic-rich shale and shale itself, and its influence on the characteristics of shale gas and organic matter pore development. *Mar. Pet. Geol.* **2022**, 140 (2022).
59. Zhang, K., Yuan, X. J. & Han, F. L. Editorial: Reservoir formation conditions and enrichment mechanisms of shale oil and gas. *Front. Earth Sci.* **10** (2023).
60. Ji, W. et al. Evolution characterization of marine shale gas occurrence state in South China. *J. Cent. S. Univ. (Sci. Technol.)* **53**(9), 3590–3602 (2022) (in Chinese with English abstract).
61. Wang, T. et al. Characteristics and influencing factors of supercritical methane adsorption in Deep Gas Shale: a case study of Marine Wufeng and Longmaxi formations from the Dongxi Area, Southeastern Sichuan Basin (China). *Energy Fuels.* **36** (3), 1531–1546 (2022).

Acknowledgements

This study was supported by the National Natural Science Foundation of China (No. 42102192), the Natural Science Foundation of Sichuan Province (No. 2024NSFSC0086), the open fund of Key Laboratory of Tectonics

and Petroleum Resources (China University of Geosciences), Ministry of Education, Wuhan (TPR-2022-08), the open fund of Shale Gas Evaluation and Exploitation Key Laboratory of Sichuan Province (YSK2022010). We sincerely appreciate all anonymous reviewers and the handling editor for their critical comments and constructive suggestions.

Author contributions

H.X.Y., Z.K. and J.S. wrote the main manuscript text, H.X.Y., J.Z.X., W.X.Y., J.W. prepared Figs. 1, 2 and 3. L.J., W.Y.J. and G.Z. prepared Figs. 4, 5, 6 and 7. T.T., Y.C., Y.X.J. and H.F.L. prepared Figs. 8, 9 and 10. W.Z.Y. and Y.L.T. prepared Figs. 8, 9 and 10. All authors reviewed the manuscript.

Declarations

Competing interests

The authors declare no competing interests.

Additional information

Correspondence and requests for materials should be addressed to K.Z.

Reprints and permissions information is available at www.nature.com/reprints.

Publisher's note Springer Nature remains neutral with regard to jurisdictional claims in published maps and institutional affiliations.

Open Access This article is licensed under a Creative Commons Attribution-NonCommercial-NoDerivatives 4.0 International License, which permits any non-commercial use, sharing, distribution and reproduction in any medium or format, as long as you give appropriate credit to the original author(s) and the source, provide a link to the Creative Commons licence, and indicate if you modified the licensed material. You do not have permission under this licence to share adapted material derived from this article or parts of it. The images or other third party material in this article are included in the article's Creative Commons licence, unless indicated otherwise in a credit line to the material. If material is not included in the article's Creative Commons licence and your intended use is not permitted by statutory regulation or exceeds the permitted use, you will need to obtain permission directly from the copyright holder. To view a copy of this licence, visit <http://creativecommons.org/licenses/by-nc-nd/4.0/>.

© The Author(s) 2025